University of Groningen

Master Project

Ferromagnetic Insulator State in Doped $FeTiO_3$

Author:
A. C. Berceanu

Supervisor:
M. Mostovoy

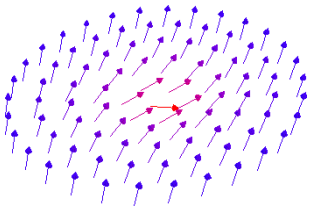

Institute for Theoretical Physics
Zernike Institute for Advanced Materials

August 19, 2008

Abstract

The solid solution (1-x)$FeTiO_3$–(x)Fe_2O_3 of the two antiferromagnetic compounds, $FeTiO_3$ (ilminite) and Fe_2O_3 (α-hematite), exhibits an unusual insulating ferromagnetic state appearing around room temperature, for a range of concentrations x between 0.2 and 0.6. We show that Fe dopants in Ti layers induce large non-collinear modulations of spins in neighboring magnetic layers. We study the properties of these spin polarons and their effect on the magnetic properties of (1-x)$FeTiO_3$–(x)Fe_2O_3. We found that co-planar spin configurations have lower energy than skyrmions. These polarons can carry a very large in-plane magnetic moment resulting in superparamagnetic behavior of the magnetic susceptibility in the antiferromagnetically ordered phase. We also explore the possibility that the long-range interactions between the spins of Fe impurities, mediated by overlapping spin polarons in neighboring magnetic layers, can give rise to an antiferromagnetic-to-ferromagnetic transition at relatively low concentrations x.

Contents

Chapter 1

Introduction

1.1 Motivation

Magnetism is a subject which has been studied for nearly three thousand years. Lodestone, an iron ore, first attracted the attention of Greek scholars and philosophers, and the navigational magnetic compass was the first technological product resulting from this study. Although the compass was certainly known in Western Europe by the twelfth century AD, it was not until around 1600 that anything resembling a modern account of the working of the compass was proposed. Progress in the last two centuries has been more rapid and two major results have emerged which connect magnetism with other physical phenomena. First, magnetism and electricity are inextricably linked and are the two components that make up light, which is an electromagnetic wave. Second, this link originates from the theory of relativity, and therefore magnetism can be described as a purely relativistic effect, due to the relative motion of an observer and charges moving in a wire, or in the atoms of iron. However, it is the magnetism in condensed matter systems, including ferromagnets, spin glasses and low dimensional systems, which is still of great interest today. Macroscopic systems exhibit magnetic properties which are fundamentally different from those of atoms and molecules, despite the fact that they are composed of the same basic constituents. This arises because magnetism is a collective phenomenon, involving the mutual cooperation of enormous numbers of particles, and is in this sense similar to superconductivity, superfluidity and even to the phenomenon of the solid state itself. The interest in answering fundamental questions runs in parallel with the technological drive to find new materials for use as permanent magnets, sensors, or in recording applications.

Solids contain magnetic moments which can act together in a cooperative way lead to behaviour that is quite different from what would be observed if all the magnetic moments were isolated from one another. This, coupled with the diversity of types of magnetic interactions that can be found, leads to a surprisingly rich variety of magnetic properties in real systems. Let us now consider a few of the different types of magnetic ground states which can be produced by these interactions.

Some of these different ground states are **ferromagnets** – Fig. 1.1, in which all the

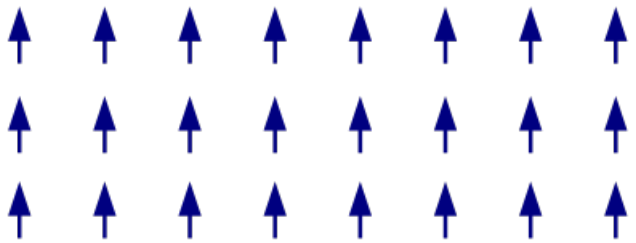

Figure 1.1: Ferromagnetic ordering. The arrows represent the magnetic moments associated with the electronic spins. Ferromagnetism is the "normal" form of magnetism, with which most people are familiar, as exhibited in horseshoe magnets and refrigerator magnets. Figure from http://en.wikipedia.org/wiki/Ferromagnetic.

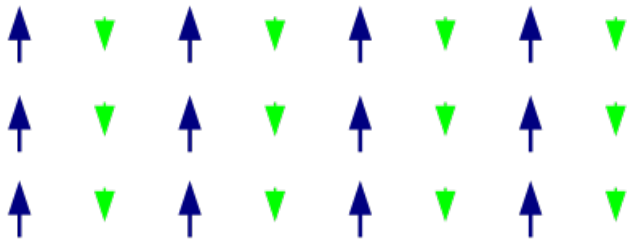

Figure 1.2: Ferrimagnetic ordering. The arrows represent the magnetic moments associated with the electronic spins. Ferrimagnetic materials are like ferromagnets in that they hold a spontaneous magnetization below the Curie temperature, and show no magnetic order (are paramagnetic) above this temperature. Figure from http://en.wikipedia.org/wiki/Ferrimagnetic.

magnetic moments (corresponding to the electron spins) are in parallel alignment, **antiferromagnets** in which adjacent magnetic moments lie in antiparallel alignment (resulting in no net magnetization), **spiral** and **helical** structures in which the direction of the magnetic moment precesses around a cone or a circle as one moves from one site to the next, and **spin glasses**, in which the magnetic moments lie in frozen random arrangements [1, 2].

A **ferrimagnetic** (Fig. 1.2) material is one in which the magnetic moments of the atoms on different sublattices are opposed, as in antiferromagnetism; however, in ferrimagnetic materials, the antiparallel moments are unequal, resulting in a net magnetization.

These alignment effects only occur at temperatures below a certain critical temperature, called the **Curie temperature** (for ferromagnets and ferrimagnets) or the **Néel temperature** (for antiferromagnets).

While ferromagnetism was known for thousands of years and usually found in (transition) metals such as Fe, Ni and Co, antiferromagnetism on the other hand was discovered much

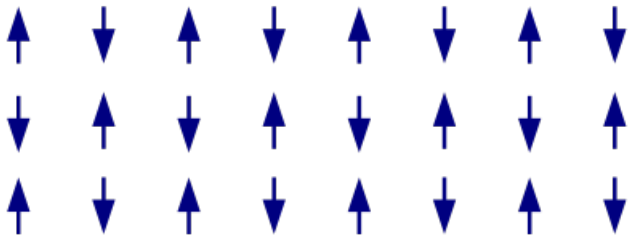

Figure 1.3: Antiferromagnetic ordering. The arrows represent the magnetic moments associated with the electronic spins. When no external field is applied, the antiferromagnetic structure corresponds to a vanishing total magnetization. In a field, a kind of ferrimagnetic behavior may be displayed in the antiferromagnetic phase, with the absolute value of one of the sublattice magnetizations differing from that of the other sublattice. Figure from http://en.wikipedia.org/wiki/Antiferromagnetic.

more recently, in the 1930's, due to its lack of measurable overall magnetization (see Fig. 1.3). Antiferromagnetism is usually found in insulators, such as NiO.

However, people are very interested in finding **insulating ferromagnets**, because of their practical applications. Since in an insulating ferromagnet one can not induce a current (by a varying magnetic field such as those used in the hard-disk industry) because of the lack of free carriers, these materials should reduce loses by dissipation. A few examples of insulating ferromagnets do exist in the literature, such as EuO and $YTiO_3$ [3], but they are usually very expensive to fabricate and thus not suitable for end-user applications.

This thesis deals with the magnetic properties of a new and easy-to-produce insulating ferromagnet.

1.2 Magnetic Interactions

In this section we consider two different types of magnetic interactions which are important in allowing the magnetic moments in a solid communicate with each other and potentially to produce long range order.

1.2.1 Superexchange

The first of these interaction mechanisms is called "superexchange", and, as we will see, it explains why some ionic solids (which are insulators) have antiferromagnetic ground states.

A number of ionic solids, including some oxides and fluorides, have magnetic ground states. For example, MnO (see Fig. 1.4) and MnF_2 are both antiferromagnets [4], though this observation appears at first sight rather surprising because there is no direct overlap

between the electrons on Mn^{2+} ions in each system. The exchange interaction is normally very short-ranged, so that the longer-ranged interaction that is operating in this case must be in some sense "super".

Let us now introduce the concept of exchange integral. Consider a simple model with just two electrons which have spatial coordinates $\boldsymbol{r}_1$ and $\boldsymbol{r}_2$, such that the first electron is in the state $\psi_a(\boldsymbol{r}_1)$ and the second in the state $\psi_b(\boldsymbol{r}_2)$. Their total wave function must be an antisymmetrized product of the individual wave functions. Hence the spin part of the wave function must either be an antisymmetric singlet state χ_S ($S = 0$) in the case of a symmetric spatial part or a symmetric triplet state χ_T ($S = 1$) in the case of an antisymmetric spatial part. Therefore we can write the wave function for the singlet case Ψ_S and the triplet state Ψ_T as

$$\Psi_S = \frac{1}{\sqrt{2}} \left(\psi_a(\boldsymbol{r}_1)\psi_b(\boldsymbol{r}_2) + \psi_a(\boldsymbol{r}_2)\psi_b(\boldsymbol{r}_1)\right) \chi_S \tag{1.1a}$$

$$\Psi_T = \frac{1}{\sqrt{2}} \left(\psi_a(\boldsymbol{r}_1)\psi_b(\boldsymbol{r}_2) - \psi_a(\boldsymbol{r}_2)\psi_b(\boldsymbol{r}_1)\right) \chi_T, \tag{1.1b}$$

where both the spatial and spin parts of the wave function are included. The energies of the two possible states are

$$E_S = \int d\boldsymbol{r}_1\, d\boldsymbol{r}_2\, \Psi_S^\star \hat{\mathcal{H}} \Psi_S \tag{1.2a}$$

$$E_T = \int d\boldsymbol{r}_1\, d\boldsymbol{r}_2\, \Psi_T^\star \hat{\mathcal{H}} \Psi_T, \tag{1.2b}$$

with the assumption that the spin parts of the wave function χ_S and χ_T are normalized. The difference between the two energies is

$$E_S - E_T = 2 \int d\boldsymbol{r}_1\, d\boldsymbol{r}_2\, \psi_a^\star(\boldsymbol{r}_1)\psi_b^\star(\boldsymbol{r}_2)\hat{\mathcal{H}}\psi_a(\boldsymbol{r}_2)\psi_b(\boldsymbol{r}_1). \tag{1.3}$$

For a singlet state $\boldsymbol{S}_1 \cdot \boldsymbol{S}_2 = -\frac{3}{4}$ while for a triplet state $\boldsymbol{S}_1 \cdot \boldsymbol{S}_2 = \frac{1}{4}$. Hence the Hamiltonian can be written in the form of an "effective Hamiltonian"

$$\hat{\mathcal{H}} = \frac{1}{4}(E_S + 3E_T) - (E_S - E_T)\boldsymbol{S}_1\boldsymbol{S}_2. \tag{1.4}$$

The first term on the right hand side is constant and can be dropped. The second term can be rewritten is we define the exchange integral (or exchange constant) J by

$$J = \frac{E_S - E_T}{2} = \int d\boldsymbol{r}_1\, d\boldsymbol{r}_2\, \psi_a^\star(\boldsymbol{r}_1)\psi_b^\star(\boldsymbol{r}_2)\hat{\mathcal{H}}\psi_a(\boldsymbol{r}_2)\psi_b(\boldsymbol{r}_1). \tag{1.5}$$

Superexchange can in fact be defined as an indirect exchange interaction between non-neighbouring magnetic ions which is mediated by a non-magnetic ion (in this case oxygen) which is placed in between the magnetic ions. It arises because there is a kinetic energy gain for antiferromagnetism, which can be understood by referring to Fig. 1.5, showing two transition metal ions separated by an oxygen ion. For simplicity we will assume that the magnetic moment on the transition metal ion is due to a single unpaired electron

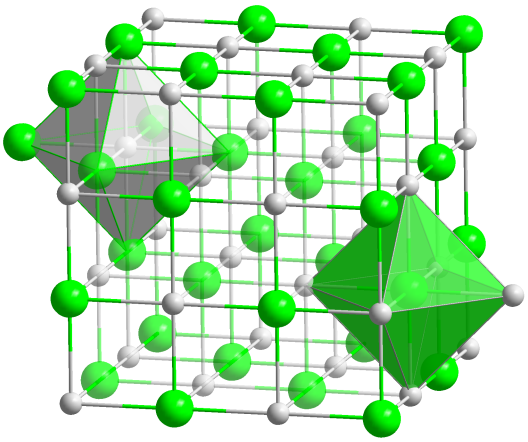

Figure 1.4: The crystal structure of MnO. Near-neighbour pairs of Mn^{2+} (green) ions are connected via O^{2-} (white) ions. MnO has a rock-salt structure, with octahedral coordination (the coordination polyhedra are also shown): each ion has 6 neighbours of the other kind. Figure from http://en.wikipedia.org/wiki/Natrium_chloride.

(more complicated cases can be dealt with in analogous ways). Hence if this system were perfectly ionic, each metal ion would have a single unpaired electron in a d orbital (depicted in gray) and the oxygen would have two p electrons in its outermost occupied states (depicted in orange). The figure demonstrates that antiferromagnetic coupling lowers the energy of the system by allowing these electrons to become delocalized over the whole structure.

Because superexchange involves the oxygen orbitals as well as those of transition metal ions, it is a second-order process and is derived from second-order perturbation theory. To be more precise, the correction to the energy is of the fourth order in powers of the $d-p$ hopping amplitude. However, since the effective amplitude of the $d-d$ hopping, $t_{dd} = t_{dp}^2/\Delta$, where Δ is the charge transfer energy, this correction is of second order in t_{dd}. A general consequence of second-order perturbation theory is that the energy involved is approximately given by the square of the matrix element of the transition divided by the energy cost of making the excited state. Here the transition matrix element is controlled by the hopping integral t, which is proportional to the bandwidth in a simple tight-binding approach[1]. The energy cost of making an excited state is given by the Coulomb energy U. Thus we have that $J \propto -t^2/U$.

The exchange integral consists of two parts. The first is a potential exchange term which represents the electron repulsion and favours ferromagnetic ground states, but is small when the ions are well separated. The second is a kinetic exchange term which dominates here and is the effect discussed above. It depends on the degree of overlap of orbitals and thus superexchange is strongly dependent upon the angle of the M-O-M bond. The figure has been drawn for one type of d orbital only, but the effect of other d orbitals which can overlap with the oxygen orbitals may also need to be added.

[1]The hopping integral is the probability amplitude for an electron to hop between neighbouring ions and is given by the matrix elements of the periodic crystal potential in the basis of ionic wave functions.

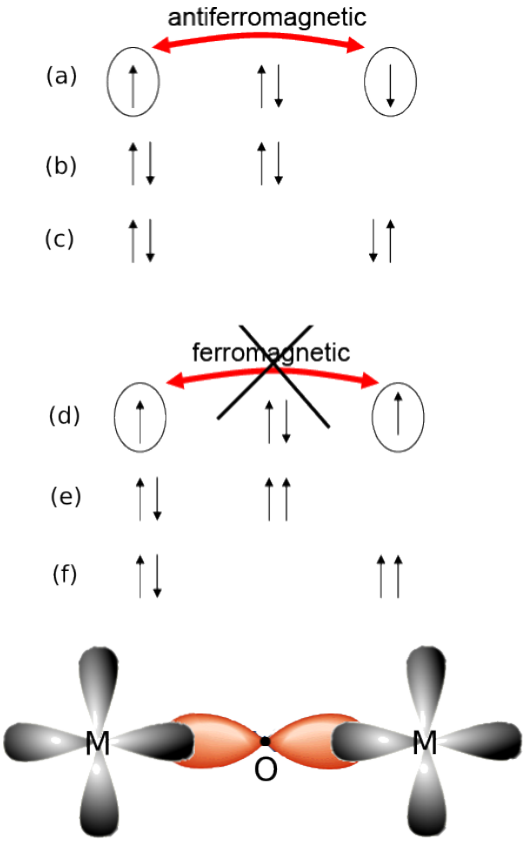

Figure 1.5: Superexchange in a magnetic oxide. The arrows show the spins of the four electrons and how they are distributed over the transition metal (M) and oxygen (O) atoms. M is assumed to have a single unpaired electron, making it magnetic. If the moments on the transition metal atoms are coupled antiferromagnetically (a,b,c), the ground state is (a) and this can mix with excited configurations like (b) and (c). The magnetic electrons can thus be delocalized over the M-O-M unit, thus lowering the kinetic energy. If the moments on the metal (M) atoms are coupled ferromagnetically (d,e,f), the ground state (d) cannot mix with excited configurations like (e) and (f) because these configurations are prevented by the Pauli exclusion principle. The ferromagnetic configuration therefore costs more energy.

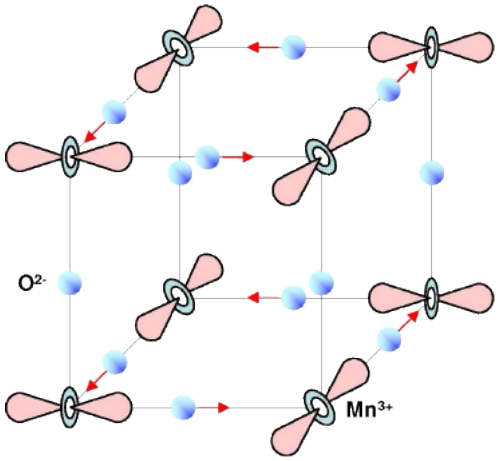

Figure 1.6: Orbital structure and shifts of oxygen ions in $LaMnO_3$. The Jahn-Teller distortion helps to minimize the total strain of the crystal. For more clearness, the oxygen and unoccupied $d_{x^2-y^2}$ orbitals are not drawn.

In some circumstances, superexchange can actually be ferromagnetic. For example, imagine a situation in which there is a coupling, through an oxygen ion, between an occupied e_g orbital on one magnetic ion and an unoccupied e_g orbital on another magnetic ion. There is an energetic advantage to the e_g electron hopping onto the unoccupied orbital, if when it arrives its spin is aligned with the spin of the t_{2g} electrons because of the Hund's rule coupling. Thus the superexchange could be ferromagnetic in this case, but this is a weaker interaction and less common than the usual antiferromagnetic superexchange.

In general, the consideration of magnetic interactions can get very complex. Therefore, Goodenough, Kanamori and Anderson[5] formulated easy rules in order to predict in the most cases the right magnetic exchange interactions. In the following the Goodenough-Kanamori-Anderson (GKA) rules will be discussed.

Goodenough-Kanamori-Anderson Rules

In order to make this discussion more concrete, we will apply the GKA rules to the particular case of $LaMnO_3$. The orbital structure of this material is shown in Fig. 1.6. $LaMnO_3$ is a cubic perovskite that contains Mn^{3+} ions and Mn^{3+} is a Jahn-Teller[4] ion. As we will see, $LaMnO_3$ shows A-type antiferromagnetic ordering, with alternately aligned ferromagnetic (100) planes.

As we have discussed above, the $d-d$ overlap occurs via bridging of the oxygen p electrons. Because of this, one has to regard the geometry of the relevant orbitals which are schematically illustrated in Fig. 1.7. Here, the oxygen p orbital is occupied by two electrons and directed towards or overlap with the Mn ion. The electrons of the Mn ($3d^4$) ion will be distributed in a difficult way: three electrons will occupy the t_{2g} levels and generate a so-called core spin of $S = 3/2$, i.e. these electrons will stay at the Mn-atomic site and create a local spin. The fourth electron instead will occupy the energetically most favorable e_g level, due to the benefit of the Jahn-Teller effect. In octahedral elongated

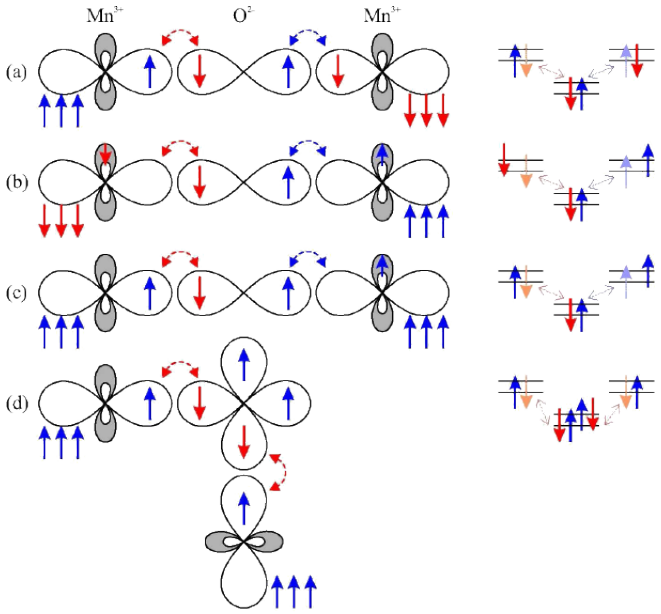

Figure 1.7: To clarify the Goodenough-Kanamori-Anderson rules, the $d_{x^2-y^2}$ (shadowed) and the d_{z^2} orbitals (to the left and right) as well as the p_z orbitals in the center of a Mn-O-Mn bond are schematically illustrated. The small arrows in the orbitals describe the itinerant electrons, the three arrows outside the orbital denote the total core spin $S = 3/2$ of the three (not shown) t_{2g} orbitals. According to the realized occupation, either an antiferromagnetic (a,b) or a ferromagnetic (c,d) coupling will be established.

systems it favors the d_{z^2} orbital and can hop. The three arrows in Figure 1.7 denotes the core spin of the three t_{2g} electrons. Here in this example, the d_{z^2} orbitals are directed towards the oxygen ions. As a result, one obtains three different options of how to occupy these orbitals, which finally leads to the three GKA rules.

The first GKA rule states that *the* 180°*-exchange between (half-)filled or empty orbitals is relatively strong and antiferromagnetic.* The conclusion of this is illustrated in Figure 1.7(a,b). Both Mn ions have one (or no) electron in their d_{z^2} orbitals. If the electrons in both Mn-O bonds hop, the itinerant spins of the adjacent Mn ions in the d_{z^2} orbitals will anti-align. Due to the strong intra-atomic Hunds coupling, the core spins have to be parallel to the according itinerant spins: i.e. the interaction between the magnetic moments of the Mn sites is antiferromagnetic.

The second GKA rule states that *when the* 180°*-exchange is due to an overlap between an occupied and an empty orbital, the resulting exchange is ferromagnetic and relatively weak.* This rule is illustrated in Figure 1.7(c). The difference from (a) is in the bond of the oxygen and the Mn ion on the right hand side. The d_{z^2} orbital of the Mn ion is empty and its orthogonal $d_{x^2y^2}$ orbital is occupied. Thus, the p electron of the oxygen can hop into the empty d_{z^2} orbital. The most energetically favorable configuration is reached when this electron will have parallel spin, according to Hunds first rule. Instead of this, the p electron on the left hand side prefers an antiferromagnetic ordering. As a result, the Mn spins order ferromagnetically.

The third GKA rule states that *the* 90°*-exchange between (half-)filled orbitals is ferromag-*

netic and relatively weak. Figure 1.7(d) shows the 90°-exchange between filled orbitals. Here, the hopping happens between a p_z orbital and the left Mn ion and between a p_y orbital and the right Mn ion. This means that two holes remain in the oxygen in the virtual intermediate state. Due to the orientation of the Mn spins, the two remaining electrons on the oxygen site have either a parallel or an antiparallel spin orientation. The intermediate state with the lowest energy will be favored. According to Hunds first rule, this is the state with parallel spin configuration of the electrons (or holes) at the oxygen site. Thus, the spins of the two Mn ions are parallel too. The energy difference between the parallel and antiparallel configuration (exchange integral) is given by:

$$J \approx \frac{2t_{dp}^4}{\Delta^2}\left(\frac{1}{2\Delta + U_p - J_H} - \frac{1}{2\Delta + U_p}\right) \approx \frac{t_{dp}^4}{\Delta^2(2\Delta + U_p)}\frac{J_H}{(2\Delta + U_p)} \tag{1.6}$$

where J_H is the Hunds coupling energy and U_p the Coulomb repulsion energy between the two p orbitals. Since the ratio J_H/U_p is usually small for such systems, ferromagnetic superexchange is relatively weak compared to the antiferromagnetic one.

With the above considerations, it is now possible to explain the magnetic ordering of $LaMnO_3$ if we assume the orbital odering shown in Figure 1.6. As we can easily see, in the horizontal plane a half-filled orbital is directed towards an unoccupied orbital, which means that the layers order ferromagnetically. Between the planes the overlapping orbitals are always empty and this leads to an antiferromagnetic ordering. Therefore an A-type antiferromagnet results.

1.2.2 Double Exchange

In some oxides, it is possible to have a ferromagnetic exchange interaction which occurs because the magnetic ion can show mixed valency, that is it can exist in more than one oxidation state. Examples include compounds containing the Mn ion which can exist in oxidation state 3 or 4, i.e. as Mn^{3+} or Mn^{4+}. One such material is $La_{1-x}Sr_xMnO_3$ ($0 \leq x \leq 1$) which adopts a perovskite structure. Sr is divalent and La is trivalent. This implies that a fraction x of the Mn ions are Mn^{4+} and $1-x$ are Mn^{3+}. The end members of the series, with $x = 0$ and $x = 1$ are both antiferromagnetic Mott insulators, as would be expected for an oxide material in which the magnetism is mediated by superexchange through the oxygen. In fact, we already discussed the case of $LaMnO_3$ in detail in the previous Section.

However, when $LaMnO_3$ is doped with Sr up to a level of $x = 0.175$, the Jahn-Teller distortion vanishes and the system becomes ferromagnetic with a Curie temperature around room temperature, below which temperature the material becomes metallic. This is clearly visible in Fig. 1.8, which shows the experimental phase diagram of $La_{1-x}Sr_xMnO_3$, taken from Ref. [6]. It is perhaps also worth mentioning that colossal magnetoresistance effects also show up in $La_{1-x}Sr_xMnO_3$ for Sr concentrations around $x = 0.3$. This is rather promising for applications.

The ferromagnetic alignment is due to the double exchange mechanism, which can be understood with reference to Fig. 1.9 [7]. The e_g electron on a Mn^{3+} ion can hop to

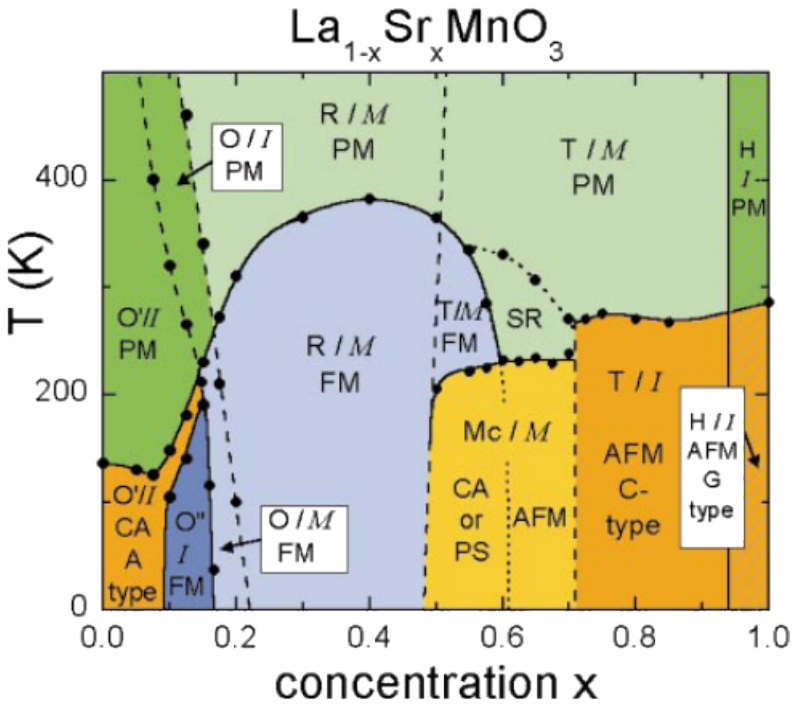

Figure 1.8: Phase diagram of $La_{1-x}Sr_xMnO_3$ for the complete concentration regime. The crystal structures (Jahn-Teller distorted orthorhombic: O′; orthorhombic: O; orbital-ordered orthorhombic: O″; rhombohedral: R; tetragonal: T; monoclinic: Mc; and hexagonal: H) are indicated as well as the magnetic structures [paramagnetic: PM (green); short-range order: SR; canted: CA; A-type antiferromagnetic structure: AFM (yellow); ferromagnetic: FM (blue); phase separated: PS; and antiferromagnetic C-type structure] and the electronic state [insulating: I (dark); metallic: M (light)]. Adapted from Ref. [6].

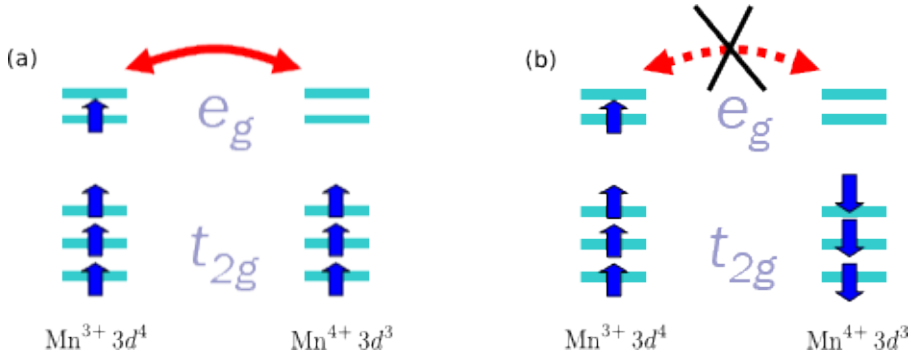

Figure 1.9: Double exchange mechanism gives ferromagnetic coupling between Mn^{3+} and Mn^{4+} ions participating in electron transfer. The d orbitals of the Mn ions can be categorised into localized t_{2g} orbitals and delocalized e_g orbitals. The single-centre exchange interaction favours hopping if (a) neighbouring ions are ferromagnetically aligned and not if (b) neighbouring ions are antiferromagnetically aligned.

a neighbouring site only if there is a vacancy there of the same spin (since hopping proceeds without spin-flip of the hopping electron). If the neighbour is a Mn^{4+} which has no electrons in its e_g shell, this should present no problem. However, there is a strong single-centre (Hund's first rule) exchange interaction between the e_g electron and the three electrons in the t_{2g} level which wants to keep them all aligned. Thus it is not energetically favourable for an e_g electron to hop to a neighbouring ion in which the t_{2g} spins will be antiparallel to the e_g electron (Fig. 1.9(b)). Ferromagnetic alignment of neighbouring ions is therefore required to maintain the high-spin arrangement on both the donating and receiving ion. The ability to hop gives a kinetic energy saving. Thus the system ferromagnetically aligns to save energy. Moreover, the ferromagnetic alignment then allows the e_g electrons to hop through the crystal and the material becomes metallic [8].

While the microscopic mechanism responsible for the **ferromagnetic metal** behaviour of $La_{1-x}Sr_xMnO_3$ is standard and very well understood, the one governing the **ferromagnetic insulator** (1-x)$FeTiO_3$–(x)Fe_2O_3 has been largely a mystery until now.

1.3 Experimental Facts

We now move on to "our" material, namely the solid solution (1-x)$FeTiO_3$–(x)Fe_2O_3. We will first discuss the properties of the end members of this series, for $x = 0$ (Section 1.3.1) and for $x = 1$ (Section 1.3.2) and then give a short overview of the interesting magnetic properties of this material, in Section 1.3.3.

1.3.1 Ilmenite

For $x = 0$, we have the compound $FeTiO_3$, which is in fact a commonly found mineral called ilmenite. This is a weak A-type antiferromagnet below a Néel temperature of only 60 K (the word "week" in this context is used only in order to emphasize the relatively low value of the critical ordering temperature).

A simplified version of the crystal structure of ilmenite is shown in Fig. 1.10. It consists of stacked hexagonal planes of alternating Fe^{2+} ($3d^6$) ions and Ti^{4+} ($3p^6$) ions. These planes are displaced by one lattice constant a with respect to one another, first in one direction and then in the opposite one, each third plane being on top of the first one (the so-called ABC stacking). The unit cell of this (rather complicated) rhombohedral crystal structure spreads across 7 layers and contains 54 atoms.

The (nearest-neighbour) in-plane interactions are ferromagnetic, while the weaker out-of-plane interactions are antiferromagnetic and due to a normal superexchange mechanism, through the oxygen ions. There are of course also next-nearest-neighbour interactions, but they are orders of magnitude smaller and can thus be neglected. Since the values of the exchange constants were determined by neutron scattering through approximately fitting magnon dispersion spectra, they should only be trusted as an order of magnitude estimate. The (absolute) values were reported to be 4.9 ± 0.2 K for the in-plane ferromagnetic interaction and 0.07 ± 0.05 K for the out-of-plane antiferromagnetic one [10].

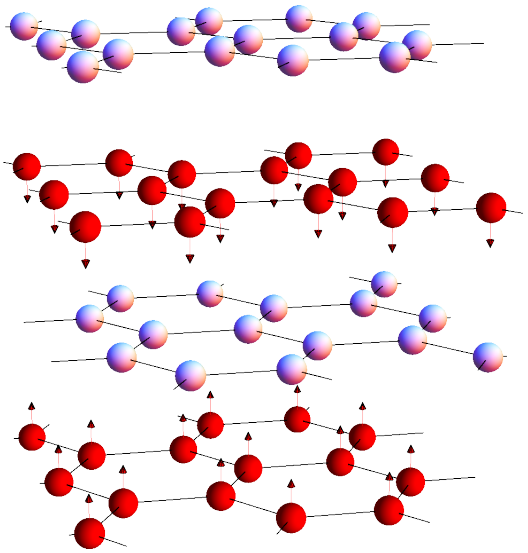

Figure 1.10: Simplified crystal structure of $FeTiO_3$ (ilmenite). The red spheres represent the magnetic Fe^{2+} ions with spin 2, while the blue/pink spheres represent the non-magnetic (spin 0) Ti^{4+} ions. The oxygen ions (which are also non-magnetic) are not shown, for simplicity. The material consists of stacked hexagonal layers of alternating Fe and Ti ions. X-ray diffraction measurements place the distance between two successive layers at $c = 2.36\,\mathring{A}$ and the edge of a hexagon at $a = 2.93\,\mathring{A}$ [9]. The (nearest-neighbour) intra-layer interactions are ferromagnetic, while the weaker inter-layer interactions are antiferromagnetic and due to a normal superexchange mechanism (through the oxygen ions). This results in an A-type antiferromagnetic ground state below a Néel temperature of only $T_c = 60$ K.

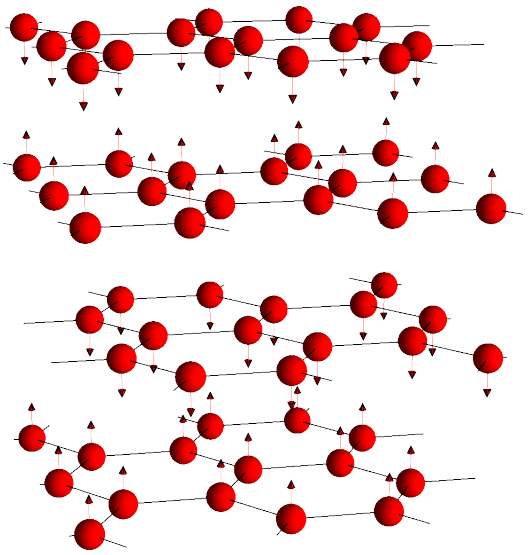

Figure 1.11: Simplified crystal structure of Fe_2O_3 (α-hematite). The red spheres represent the magnetic Fe^{3+} ions with spin 3/2. The oxygen ions (which are non-magnetic) are not shown, for simplicity. The material consists of stacked hexagonal layers of Fe ions. X-ray diffraction measurements place the distance between two successive layers at $c = 2.36\,\mathring{A}$ and the edge of a hexagon at $a = 2.93\,\mathring{A}$ [9]. The (nearest-neighbour) intra-layer interactions are ferromagnetic, while the stronger inter-layer interactions are antiferromagnetic. There exists also an second-order (next-nearest-neighbour) antiferromagnetic interaction between planes, due to a normal superexchange mechanism (through the oxygen ions). The ground state is again an A-type antiferromagnet below a Néel temperature of $T_c = 950$ K.

1.3.2 Alpha-Hematite

For $x = 1$, we have the compound Fe_2O_3, which is also an abundant mineral known under the name of α-hematite. The name hematite is derived from the Greek word for blood (haima) because hematite can be red, as in rouge, a powdered form of hematite. The color of hematite lends itself well to use as a pigment. Hematite crystallizes in the rhombohedral system, and it has the same crystal structure as ilmenite. Hematite and ilmenite actually form a homogeneous solid solution at temperatures above 950 °C.

Hematite is also an A-type antiferromagnet below a Néel temperature of 950 K. Its crystal structure is depicted in a simplified manner in Fig. 1.11. Since the distance between successive magnetic planes is now twice smaller than it was in the case of ilmenite, it follows logically that hematite should be a much stronger antiferromagnet. This is confirmed by the large value of its critical ordering temperature.

As we have already mentioned, the crystal structure of hematite consists of stacked hexagonal planes of Fe^{3+} ($3d^5$) ions. As in the case of ilmenite, these planes are displaced by one lattice constant a with respect to one another, first in one direction and then in the opposite one, each third plane being on top of the first one.

The (nearest-neighbour) in-plane interactions are ferromagnetic, with an absolute value of the exchange constant of 0.98 ± 0.25 K [10]. The stronger out-of-plane antiferromagnetic

interactions are reported to have an absolute value of the exchange constant of 31.7 ± 0.62 K. There is also a second-order (next-nearest-neighbour) antiferromagnetic interaction between planes, due to a normal superexchange mechanism through the oxygen ions. Its exchange constant is, as in the case of ilmenite, 0.07 ± 0.05 K [10].

1.3.3 Magnetic Properties of the Solid Solution

As we already mentioned, ilmenite and hematite form a complete solid solution at temperatures above 950 °C. Let us see what happens in practice.

If one starts with $FeTiO_3$ ($x = 0$) and then adds a small amount x of Fe_2O_3, the Fe^{3+} ions start to replace some of the Ti^{4+} ions in the intermediate layers. Due to the valence difference between Fe^{3+} and Ti^{4+}, charge doping is induced by this substitution

$$Ti^{4+}\, Fe^{2+} \rightarrow 2Fe^{3+}. \tag{1.7}$$

However, unlike manganites, the charge doping does not make this solid solution metallic, which is why we assume that the induced charge is localized by the impurity that donated it and neglect charge degrees of freedom.

The Fe^{3+} impurities align the moments on the adjacent Fe^{2+} ions (above and below) parallel to each other by the strong nearest-neighbour antiferromagnetic interactions. By gradually increasing the concentration x, one can get continuously to the other end of the series, Fe_2O_3 ($x = 1$).

It is clear that for very small and very large concentrations the system will be an A-type antiferromagnet. The experimental phase diagram for a range of concentrations x between 0 and 0.45, as a function of absolute temperature, is presented in Fig. 1.12.

The compound shows an extended paramagnetic phase which lacks long-range order and is depicted here in orange, but also a superparamagnetic phase (yellow), also disordered and characterized by large amplitude fluctuations of the magnetization. Superparamagnets in general show induced magnetic behavior that follows a Curie type law but with exceptionally large values for the Curie constants. For small concentrations and temperatures we of course have the A-type antiferromagnetic phase characteristic of $FeTiO_3$ (blue). There is also quite an extended spin-glass phase at low temperatures (red), which is still unexplained. A spin glass is a disordered material exhibiting high magnetic frustration. Frustration is the inability of the system to remain in a single lowest energy state (the ground state). The typical origin of this property is the simultaneous presence of competing interactions and disorder. Spin glasses have many ground states which are never explored on experimental time scales. One can say that the system is in a state of frozen disorder.

The crucial point about this phase diagram, however, is the presence of an extended **ferrimagnetic insulating** phase (green), which starts at relatively low concentrations of $x \approx 0.15$. The goal of this thesis is to understand this phase diagram from a theoretical point of view, with a particular emphasis on the superparamagnetic and ferrimagnetic phases.

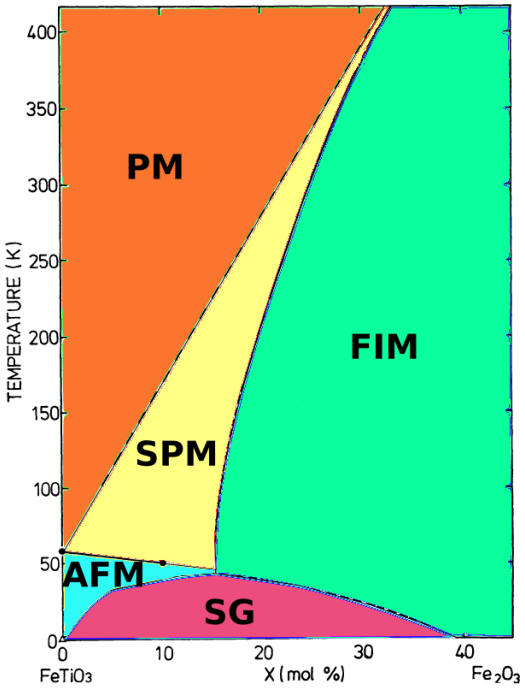

Figure 1.12: Experimental magnetic phase diagram of the solid solution (1-x)$FeTiO_3$–(x)Fe_2O_3, for a range of concentrations x between 0 and 0.45. The magnetic structures [paramagnetic: PM (orange); superparamagnetic: SPM (yellow); A-type antiferromagnetic structure: AFM (blue); ferrimagnetic: FIM (green); and spin-glass structure: SG (red)] are indicated. The compound is insulating throughout this whole range of concentrations. Figure adapted from Ref. [10].

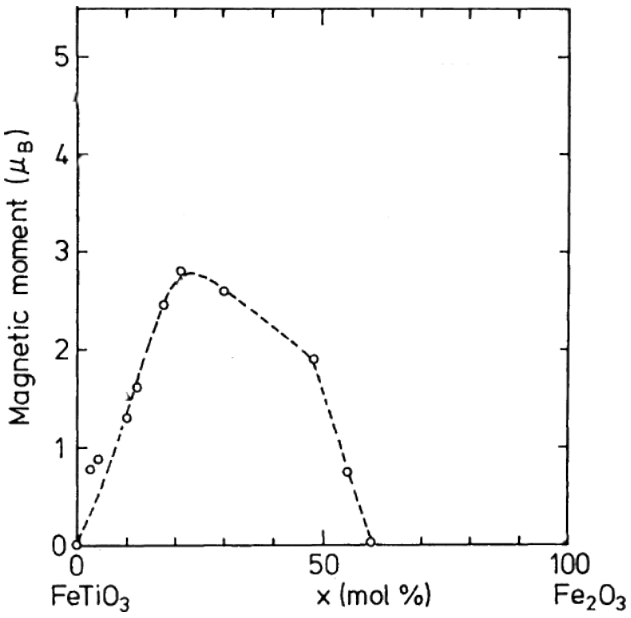

Figure 1.13: Saturation magnetization (measured in Bohr magnetons μ_B per Fe atom) of (1-x)$FeTiO_3$–(x)Fe_2O_3, for the full range of concentrations. The open circles are the experimental points, measured on polycrystalline samples. The dashed line is a fit through all the data points. A weak external magnetic field of 20 kOe was applied. Figure adapted from Ref. [10].

Before we proceed, it is also instructive to look at an experimental plot of the magnetization as a function of concentration, shown in Fig. 1.13.

As expected, the magnetization at $x = 0$ and $x = 1$ vanishes, because the system is antiferromagnetic. It increases as we approach the ferrimagnetic region, reaches a maximum around $x \approx 0.2$ and then decreases again at higher concentrations. This is also consistent with the phase diagram of Fig. 1.12.

1.4 Skyrmions

In this Section we will introduce the concept of skyrmion and see how they appear in the literature, in different contexts varying from high-energy to condensed-matter physics. But first let's see how skyrmions can be connected to our problem, namely the magnetic properties of (1-x)$FeTiO_3$–(x)Fe_2O_3.

Let us now consider only three layers of $FeTiO_3$, for simplicity. We start with the $x = 0$ case and want to see what happens for small concentrations $x \ll 1$. The corresponding illustration is sketched in Fig. 1.14.

As already noted in Section 1.3.3, if one starts with $FeTiO_3$ and then adds a small amount x of Fe_2O_3, the Fe^{3+} ions start replacing the Ti^{4+} ions in the middle layer. These Fe^{3+} ions align the moments on the adjacent Fe^{2+} ions (above and below) parallel to each other by the strong nearest-neighbour antiferromagnetic interactions. This is the case

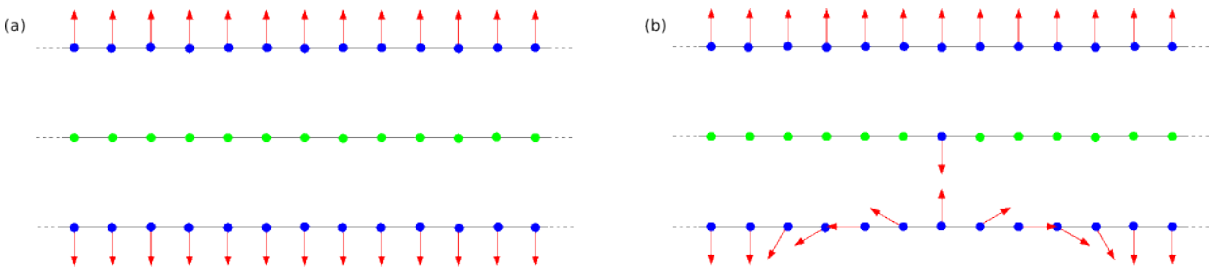

Figure 1.14: Three layers of $FeTiO_3$, side view. The blue discs represent the Fe ions, and the green ones represent the non-magnetic Ti ions. The red arrows show the direction of the spins on the Fe ions. The figure (a) corresponds to the case of $x = 0$, and (b) is shown for a very small concentration x, such that one of the Fe ions belonging to Fe_2O_3 replaced one of the Ti ions in the middle layer. The resulting spin texture is reminiscent of a skyrmion.

in Fig. 1.14(b), where we considered the limiting case of just one Ti ion which is being replaced in the center of the middle layer. From now on, we will refer to these Fe ions which replace the Ti as "impurities" and also neglect the valence difference between them and the Fe ions inside the Fe layers. Far away from the center, at infinity, in order to satisfy the antiferromagnetic interaction between the upper and the lower Fe layer, the spins will be anti-aligned. Therefore we expect a continuous rotation of the Fe spins over the angle ranging from 0 in the center to π at infinity in one of the two layers (in the case of Fig. 1.14(b), we chose the lower layer). This situation is reminiscent of the formation of a skyrmion, therefore it is instructive to briefly discuss these topological states and the various contexts of their appearance in the following sections. Before we proceed, we should note that we threat the spins of the Fe ions as classical (as opposed to quantum) spins throughout this thesis and set *all* their values to 1. The relatively large value of their spin quantum numbers makes this approximation justified.

1.4.1 In High-Energy Physics

Since the 1950's, people have attempted to explain particles in Quantum Field Theory in terms of localized field configurations. Skyrme provided an original solution to the problem of constructing fermions from bosons – see Fig. 1.15 – formulating the first topological soliton model of the nucleon in 1961 [11]. He described baryons (nuclear particles) as localized states within a nonlinear field theory.

Tony Hilton Royle Skyrme, (1922-1987) was a British physicist, best known for formulating the first topological soliton to model a particle, the **skyrmion**. A skyrmion is a homotopically non-trivial classical solution of a nonlinear sigma model with a non-trivial target manifold topology: a particular case of a topological soliton. Here, the non-linearity comes from the condition

$$\left(\pi^{+}\right)^{2} + \left(\pi^{0}\right)^{2} + \left(\pi^{-}\right)^{2} + \sigma^{2} = \text{const}, \tag{1.8}$$

where π and σ are the pi- and sigma- meson fields. Since the finite-energy requirement

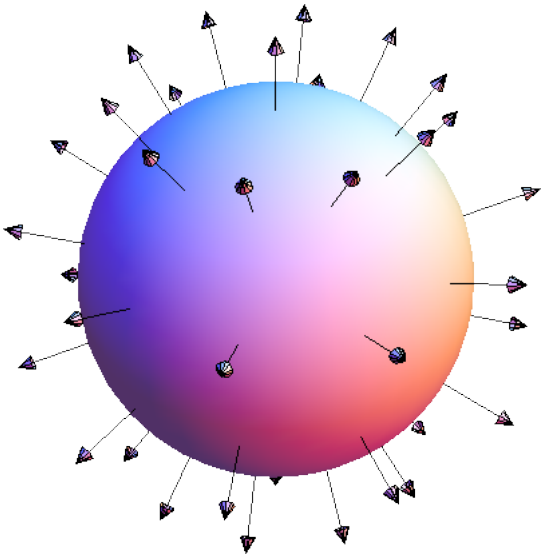

Figure 1.15: Artist illustration of a skyrmion in nuclear physics. The arrows represent the pion (spinless subatomic particles) fields and the sphere represents a baryon (which are fermions).

compactifies $\mathcal{R}^3$ to $\mathcal{S}^3$, both space and group manifolds have the topology of a three-sphere.

Generally speaking, a topological soliton or a topological defect is a solution of a system of partial differential equations or of a quantum field theory that can be proven to exist because the boundary conditions entail the existence of homotopically distinct solutions. Typically, this occurs because the boundary on which the boundary conditions are specified has a non-trivial homotopy group which is preserved by differential equations; the solutions to the differential equations are then topologically distinct, and are classified by their homotopy class. Topological defects are not only stable against small perturbations, but cannot decay or be undone or be de-tangled, precisely because there is no continuous transformation that will map them (homotopically) to a uniform or "trivial" solution.

By definition, two solutions which cannot be continuously deformed into each other are said to belong to different **homotopical classes**.

Skyrmions are also encountered in condensed matter systems in the presence of external fields or with the proliferation of topological defects. However, while in high-energy physics skyrmions are mappings of four-dimensional pion fields $(\pi^+, \pi^0, \pi^-, \sigma)$ on three-dimensional spaces, in the context of condensed matter they are mappings of three-dimensional fields on two spatial dimensions.

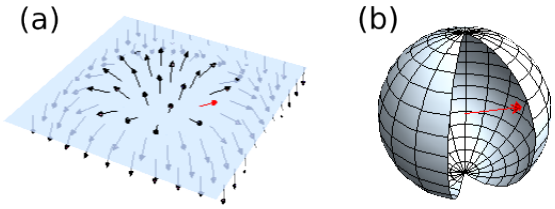

Figure 1.16: The mapping $\boldsymbol{n}(\boldsymbol{x})$ between the (x_1, x_2) coordinate plane (a) and the $\mathcal{S}^2$ spin-space sphere (b). Since the coordinate plane can be compactified, it is equivalent to another sphere. A skyrmion with $q = 1$ is on the plane, and the position of the red spin is shown on the sphere.

1.4.2 In Condensed Matter Physics

2D Heisenberg Ferromagnet

The Hamiltonian for a classical[2] two-dimensional Heisenberg ferromagnet, in the continuous limit, reads:

$$H = \int d^2\boldsymbol{x}\, \partial_\alpha n_\beta(\boldsymbol{x}) \partial^\alpha n^\beta(\boldsymbol{x}) \tag{1.9}$$

Here, $\boldsymbol{n}$ is a three-dimensional unit vector which describes the spin direction. In spherical coordinates, the values of $\boldsymbol{n}$ can be thought of as points on a two-sphere, characterized by the angles θ and ϕ:

$$\boldsymbol{n} = (\cos\theta, \sin\theta\cos\phi, \sin\theta\sin\phi) \tag{1.10}$$

This vector has values for each point of the $\boldsymbol{x} = (x_1, x_2)$ coordinate plane: $\boldsymbol{n} = \boldsymbol{n}(\boldsymbol{x})$. To get a finite energy, its gradient should vanish at infinity. This condition implies that $\boldsymbol{n}$ should have a constant value at infinity, which can be chosen arbitrarily, for example:

$$\boldsymbol{n}(\boldsymbol{x}) \to (-1, 0, 0) \quad \text{as} \quad |x| \to \infty \tag{1.11}$$

Because all the points of the (x_1, x_2) plane have the same value at infinity, we can compactify this plane into a sphere, and all these points will correspond to the "north pole" of this sphere. Therefore we can think of $\boldsymbol{n}(\boldsymbol{x})$ as a mapping between two spheres, the sphere compacted from the coordinate space and the one in the spin-space (see Fig. 1.16).

Two such mappings $\boldsymbol{n}_1$ and $\boldsymbol{n}_2$ belong to different homotopical classes if they cannot be continuously deformed into one another. There are of course an infinite number of such classes, which can be classified by their degree of mapping, also known as **topological charge** (or Pontryagin index). The topological charge is usually denoted by q and defined as

$$q = \frac{1}{8\pi} \int d^2\boldsymbol{x} \epsilon_{\alpha\beta\gamma}\epsilon_{\mu\nu} n^\alpha \frac{\partial n^\beta}{\partial x_\mu} \frac{\partial n^\gamma}{\partial x_\nu}, \tag{1.12}$$

with $\epsilon_{\mu\nu}$ being the Levi-Civita symbol in two dimensions. Also, Einstein's summation convention was used in Eq. (1.12). This rather complicated expression acquires a very simple and intuitive meaning if one transforms it to spherical coordinates:

$$q = \frac{1}{4\pi} \int \sin\theta(\boldsymbol{x}) d\theta(\boldsymbol{x}) d\phi(\boldsymbol{x}). \tag{1.13}$$

[2]The long-wavelength fluctuations of interest do not depend on quantum effects

Now we see that q is just the total solid angle divided by 4π. A nice geometrical interpretation of this result is shown in Fig. 1.17. We start at the centre of the plane with the spin pointing up (towards the north pole of the sphere). As we move concentrically outwards towards the edges of the plane, the mapping $\boldsymbol{n}$ starts covering the sphere. A rotation by π radians in the plane covers the whole sphere once, corresponding to $q = 1$. Of course, one can continue and cover the sphere once more, this time from the south pole towards the north pole, and this will correspond to $q = 2$. And so on, q can be any integer, corresponding to the number of windings of the spins from $-\infty$ to $+\infty$.

The Russian physicists Alexander A. Belavin and Alexander M. Polyakov have shown [12] that the lowest value of the energy in each homotopical class is equal to

$$H = \int d^2\boldsymbol{x} \left(\frac{\partial n^\alpha}{\partial x_\mu} \right)^2 = 8\pi q. \tag{1.14}$$

It is reached for self-dual spin configurations:

$$\frac{\partial n^\alpha}{\partial x_\mu} = \pm \epsilon_{\alpha\beta\gamma} \epsilon_{\mu\nu} n^\beta \frac{\partial n^\gamma}{\partial x_\mu}. \tag{1.15}$$

Obviously, the lowest energy will be the one corresponding to the case $q = 0$. In fact, what Belavin and Polyakov proved is that such a ferromagnet has inhomogeneous metastable states (the above skyrmions, which are topologically protected), meaning that there is a finite correlation length in the system and thus no phase transition, even at very low temperatures. This of course is in accordance with the Mermin-Wagner theorem, which states that continuous symmetries cannot be spontaneously broken at finite temperature in one and two dimensional theories.

Quantum Hall Systems

Recently, skyrmions were also mentioned as possible excitations in the quantum Hall effect [13].

Of all the new physics generated by the highly perfect two-dimensional electron systems, the quantum Hall effects, integer and fractional, with their richness and complexity are perhaps the most active and exciting. The fractional quantum Hall effect is the manifestation of a new state of electron matter - a peculiar, uniform incompressible liquid phase, observed at low temperatures and in the presence of a strong magnetic field perpendicular to the two-dimensional electron layers. Part of the intellectual fascination with the quantum Hall effect phases stems from the challenge of finding new concepts to describe their properties.

At a precise value of the magnetic field (Landau level filling factor $\nu = 1$), the two-dimensional electrons condense into a fully ferromagnetic aligned quantum Hall state: the electronic system is an itinerant ferromagnet with a quantized Hall resistivity.

The low-energy electron-spin dynamics of this quantum Hall ferromagnet is extremely unusual because of the subtle interplay between Coulomb interaction among electrons

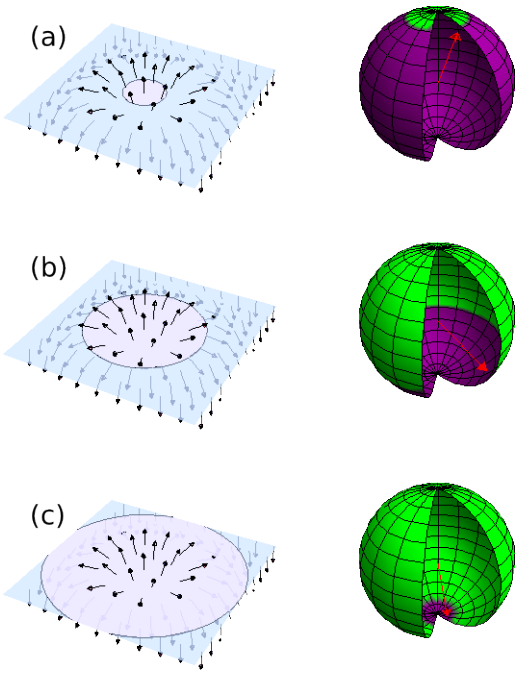

Figure 1.17: Illustration of the meaning of topological charge: (a) start at the centre of the plane with the spin pointing up. As we move concentrically outwards towards the edges of the plane (b), the mapping $\boldsymbol{n}$ starts covering the sphere. A rotation by π radians in the plane covers the whole sphere once (c), corresponding to $q = 1$.

and Zeeman coupling of electronic spins to the external magnetic field. The elementary excitations are thought to be skyrmions. Qualitatively novel physics arises, moreover, because these topological spin excitations carry electrical charge. The charge density of spin textures in quantum Hall systems is proportional to the topological charge density. Skyrmions are stabilized by Coulomb interactions, which favor a large radius, while the Zeeman energy favors a small radius.

Chapter 2

Effective Model

In this Chapter, we will first introduce a discrete model Hamiltonian for our system, using a number of simplifying approximations. We will then derive a number of interesting properties for the ground state of the system, which follow directly from the form of the Hamiltonian (Section 2.1). Finally, in Section 2.2, we will deduce a functional form for the energy of the system in the continuum approximation, starting from the discrete Hamiltonian.

We can now write the Hamiltonian of the discrete model. Consider two infinite spin layers with a square lattice, with one magnetic impurity in between. Let us label the upper plane with an index $\sigma = +1$ and the lower one with $\sigma = -1$ (see Fig. 2.1). There are three couplings in this system: a ferromagnetic in-plane, nearest-neighbor coupling described by $J_{\parallel}$, an antiferromagnetic coupling between spins from the bottom and the top layer described by $J_{\perp}$ and the antiferromagnetic interaction of the impurity spin with the spins directly above and below it, J_{imp}. Therefore we can decompose the Hamiltonian into 3 parts, accordingly:

$$H = H_{\text{intralayer}} + H_{\text{interlayer}} + H_{\text{impurity}} \tag{2.1}$$

The intralayer part of the Hamiltonian wants to align the spins in the same layer ferromagnetically (the factor 1/2 avoids double counting):

$$H_{\text{intralayer}} = -\frac{J_{\parallel}}{2} \sum_{\boldsymbol{r},\boldsymbol{\delta},\sigma} \boldsymbol{S}_{\boldsymbol{r},\sigma} \boldsymbol{S}_{\boldsymbol{r}+\boldsymbol{\delta},\sigma} \tag{2.2}$$

Here the vector index $\boldsymbol{r}$ runs over the positions of each spin in the layer and the sum over δ's is a sum over that spin's 4 in-plane nearest neighbors.

The interlayer part wants to anti-align spins from neighboring layers:

$$H_{\text{interlayer}} = -J_{\perp} \sum_{\boldsymbol{r}} \boldsymbol{S}_{\boldsymbol{r},+1} \boldsymbol{S}_{\boldsymbol{r},-1} \tag{2.3}$$

And finally, there is the interaction with the impurity:

$$H_{\text{impurity}} = -J_{\text{imp}} \boldsymbol{S}_{\text{imp}} \left(\boldsymbol{S}_{\boldsymbol{0},+1} + \boldsymbol{S}_{\boldsymbol{0},-1} \right) \tag{2.4}$$

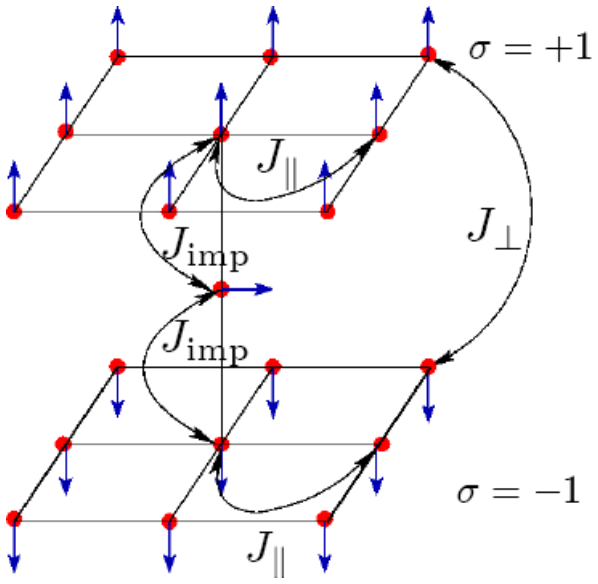

Figure 2.1: Graphical representation of the discrete lattice model.

Our sign convention dictates that $J_{\parallel} > 0$ (FM) and $J_{\perp}$, $J_{\text{imp}} < 0$ (AFM) and from experiment (see Section 1.3) we know that there is about an order of magnitude difference between these interactions:

$$|J_{\text{imp}}| \gg J_{\parallel} \gg |J_{\perp}| \,. \tag{2.5}$$

2.1 Ground State Properties

In this section we discuss the ground state of the Hamiltonian defined by Eq. (2.1). We were able to rigorously prove a number of properties of this state. We will first prove that the ground state favours co-planar spin configurations (Section 2.1.1) and then that the ground state of the system should be symmetric.

2.1.1 Plane Rotor

We begin by showing that skyrmions cannot be the ground state of the single-impurity Hamiltonian (2.1) and that the topological charge of the ground state must be 0. We then prove that all spins from the minimal-energy configuration are coplanar.

We have proven exactly that the ground state cannot be a skyrmion and must be a non-topological state with topological charge $q = 0$. That is because the spins must all lie on parallel planes. As a consequence, we are now effectively dealing with a plane-rotor (XY) model for the spins in the ground state. As opposed to a skyrmion, where one has to parametrize the spin rotation in terms of two angles (in spherical coordinates) θ and ϕ, in our case we only need one angle (we denote it by θ).

The proof is as follows. We decompose every vector $\boldsymbol{S}$ into a component parallel to the $\hat{\boldsymbol{z}}$ axis, denoted by $S_{\parallel}$, and a component perpendicular to this axis, denoted by $S_{\perp}$ (see

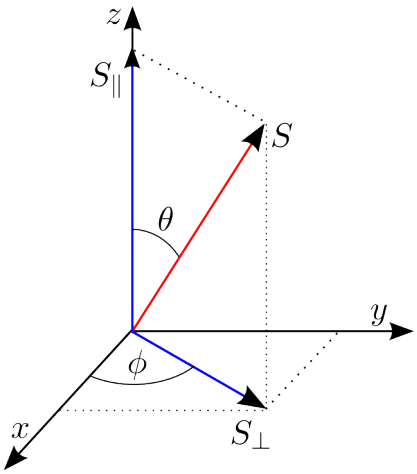

Figure 2.2: We can decompose every spin into a component along the $\hat{\boldsymbol{z}}$, denoted by $S_\parallel$, and another component perpendicular to the $\hat{\boldsymbol{z}}$ axis, along the radial direction in the xy-plane, denoted by $S_\perp$.

Fig. 2.2):

$$\boldsymbol{S} = S_\parallel \hat{\boldsymbol{z}} + S_\perp \hat{\boldsymbol{r}}. \tag{2.6}$$

Here $\hat{\boldsymbol{r}}$ is a unit vector in the xy-plane. Substituting this into Eq. (2.2), we get

$$H_{\text{intralayer}} = -\frac{J_\parallel}{2} \sum_{\boldsymbol{r},\boldsymbol{\delta},\sigma} \left(S^\parallel_{\boldsymbol{r},\sigma} S^\parallel_{\boldsymbol{r}+\boldsymbol{\delta},\sigma} + S^\perp_{\boldsymbol{r},\sigma} S^\perp_{\boldsymbol{r}+\boldsymbol{\delta},\sigma} \cos\left(\phi_{\boldsymbol{r},\sigma} - \phi_{\boldsymbol{r}+\boldsymbol{\delta},\sigma}\right) \right). \tag{2.7}$$

The first term in the round brackets has no angular dependence. In order to minimize the energy, we have to maximize the second term, which we can do without changing the first one, by imposing the condition that the cosine equals 1. This, in turn, implies that, for each of the two layers, each spin has the same angle ϕ with respect to the $\hat{\boldsymbol{x}}$ axis as any of its four neighbors:

$$\phi_{\boldsymbol{r},\sigma} = \phi_{\boldsymbol{r}+\boldsymbol{\delta},\sigma}, \quad \forall\, \sigma, \boldsymbol{r}, \boldsymbol{\delta}. \tag{2.8}$$

This means that all the spins will point in the same direction in the xy-plane.

Furthermore, substituting Eq. (2.6) into Eq. (2.3) and using a similar reasoning to the one above, we get that

$$\phi_{\boldsymbol{r},+1} = \pi + \phi_{\boldsymbol{r},-1}, \quad \forall\, \boldsymbol{r} \tag{2.9a}$$

$$\theta_{\boldsymbol{r},+1} = \pi - \theta_{\boldsymbol{r},-1}, \quad \forall\, \boldsymbol{r} \tag{2.9b}$$

which means that in the ground state, the $S_\perp$ projections in the two layers will be anti-parallel, as we expect. This completes our proof.

It is perhaps worth mentioning that the Hamiltonian is $O(3)$ symmetric (one can rotate all the spins by the same angle and still get the same energy, since the scalar products only depend on the relative angle between spins). Therefore the plane in which spins lie is determined by spontaneous breaking of the rotational symmetry.

Since skyrmions obey the boundary conditions, there is no reason why they should not be present in this system. They are, however, topological excitations rather than minimal-energy spin configurations.

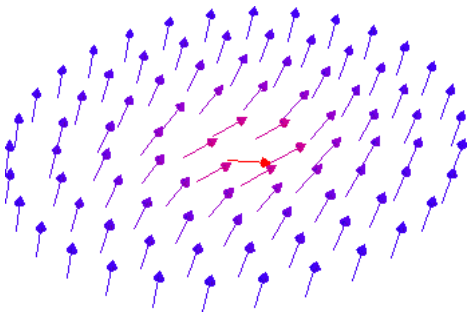

Figure 2.3: In order to lower the in-plane ferromagnetic energy, it is favourable for the spins in our polaron to lie in parallel planes (parallel to the plane of the paper in this figure). Hence the rotation of the spins in this case can be parametrized by just one angle θ.

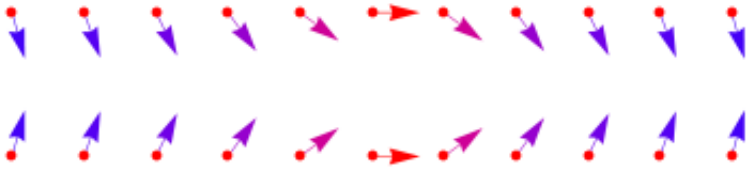

Figure 2.4: The side view of the symmetric ground state configuration. As in Fig. 2.3, the spins are coloured proportional to their deviation from the vertical axis.

2.1.2 Symmetry Considerations

We have also proven that the ground state should be symmetric.

Until now we assumed that in one of the layers, while we move from infinity towards the impurity, spins rotate from 0 to π, while in the other layer they do not rotate at all. It is easy to prove that in the actual ground state, minimizing the energy, this rotation should be equally distributed between the 2 layers. This means that, e.g. in the upper layer, while we move from infinity to the impurity, spins rotate from 0 to $\pi/2$ and in the lower layer as we move back from the impurity to infinity, they rotate from $\pi/2$ to π, making the total rotation of π required by the antiferromagnetic coupling between the layers (see Fig. 2.4). In other words, if the angle of a certain spin at distance r from the center in the upper layer with respect to the $\hat{\boldsymbol{x}}$ axis is $\theta_{\boldsymbol{r}}$ (Fig. 2.6), then the corresponding angle in the lower layer (with respect to the same axis) will be $\pi - \theta_{\boldsymbol{r}}$ (see Fig. 2.5).

The proof is as follows. We first use the main result of Section 2.1.1 and perform a

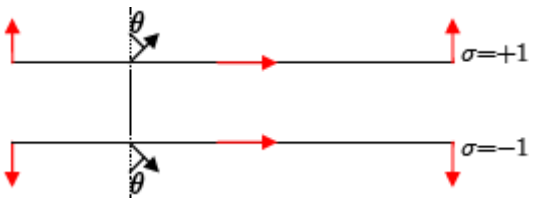

Figure 2.5: Illustration of angular parametrization, showing also symmetry of the ground state. Side view.

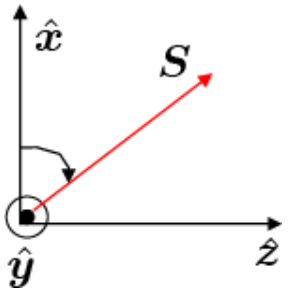

Figure 2.6: System of coordinates chosen such that the spins all lie in the xz plane. The angle θ is measured with respect to the $\hat{\boldsymbol{x}}$ axis, which is chosen perpendicular to the direction of the impurity.

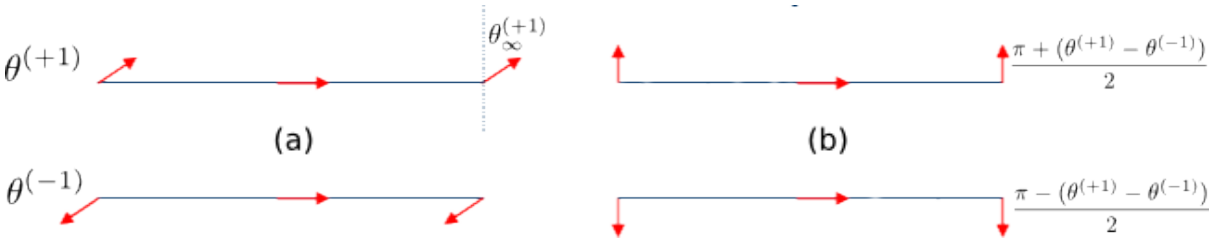

Figure 2.7: Illustration used to prove the symmetry of the ground state. Side view of the system of two spin layers. The red arrows depict the direction of the spins in the centre of the layers and at infinity. (a) Arbitrary spin configuration, in which we denote the angles between the spins in upper layer and the vertical axis (at position $\boldsymbol{r}$) by $\theta_{\boldsymbol{r}}^{(+1)}$ and the ones in the lower layer by $\theta_{\boldsymbol{r}}^{(-1)}$. (b) Symmetrized spin configuration, obtained from (a). We want to compare the energies of these two configurations.

coordinate rotation around the $\hat{\boldsymbol{z}}$ axis, such that all spins lie in the xz plane. Now let's consider two spin configurations, denoted by (a) and (b) and depicted in Figure 2.7. We denote the angular dependence of the spins in each layer by using the layer index σ as a superscript. We now want to compare the energy of an arbitrary spin configuration Fig. 2.7(a) with a symmetrized one Fig. 2.7(b). We denote the angle between the $\hat{\boldsymbol{x}}$ axis and the spin at infinity in the upper layer of configuration (a) by $\theta_\infty^{(+1)}$. We can now write the boundary conditions for state (a)

$$\theta_0^{(+1)} = \theta_0^{(-1)} = \frac{\pi}{2} \tag{2.10a}$$

$$\theta_\infty^{(-1)} = \pi + \theta_\infty^{(+1)} \tag{2.10b}$$

where the subscript 0 denotes the center of the layer ($\boldsymbol{r} = 0$). Doing the same for the symmetric state (b) yields

$$\frac{\pi + (\theta_0^{(+1)} - \theta_0^{(-1)})}{2} = \frac{\pi - (\theta_0^{(+1)} - \theta_0^{(-1)})}{2} = \frac{\pi}{2} \tag{2.11a}$$

$$\frac{\pi + (\theta_\infty^{(+1)} - \theta_\infty^{(-1)})}{2} = 0 \tag{2.11b}$$

$$\frac{\pi - (\theta_\infty^{(+1)} - \theta_\infty^{(-1)})}{2} = \pi \tag{2.11c}$$

The energies of the two configurations from Fig. 2.7 can be easily obtained from the Hamiltonian

$$\begin{aligned} E_{(a)} =& - J_\perp \sum_{\boldsymbol{r}} \cos(\theta_{\boldsymbol{r}}^{(+1)} - \theta_{\boldsymbol{r}}^{(-1)}) \\ & - J_\parallel \sum_{\boldsymbol{r},\,\boldsymbol{\delta}} \left(\cos(\theta_{\boldsymbol{r}}^{(+1)} - \theta_{\boldsymbol{r}+\boldsymbol{\delta}}^{(+1)}) + \cos(\theta_{\boldsymbol{r}}^{(-1)} - \theta_{\boldsymbol{r}+\boldsymbol{\delta}}^{(-1)}) \right) \\ E_{(b)} =& - J_\perp \sum_{\boldsymbol{r}} \cos \left[\frac{\pi + (\theta_{\boldsymbol{r}}^{(+1)} - \theta_{\boldsymbol{r}}^{(-1)})}{2} - \frac{\pi - (\theta_{\boldsymbol{r}}^{(+1)} - \theta_{\boldsymbol{r}}^{(-1)})}{2} \right] \\ & - J_\parallel \sum_{\boldsymbol{r},\,\boldsymbol{\delta}} 2 \cos \left(\frac{\theta_{\boldsymbol{r}}^{(+1)} - \theta_{\boldsymbol{r}}^{(-1)}}{2} + \frac{\theta_{\boldsymbol{r}+\boldsymbol{\delta}}^{(-1)} - \theta_{\boldsymbol{r}+\boldsymbol{\delta}}^{(+1)}}{2} \right) \end{aligned} \tag{2.12}$$

It is easy to see that the first sums in these two expressions are the same. The energy difference is

$$\begin{aligned} E_{(a)} - E_{(b)} =& \\ &= -J_\parallel \sum_{\boldsymbol{r},\,\boldsymbol{\delta}} \left[\cos(\theta_{\boldsymbol{r}}^{(+1)} - \theta_{\boldsymbol{r}+\boldsymbol{\delta}}^{(+1)}) + \cos(\theta_{\boldsymbol{r}}^{(-1)} - \theta_{\boldsymbol{r}+\boldsymbol{\delta}}^{(-1)}) - 2 \cos \left(\frac{\theta_{\boldsymbol{r}}^{(+1)} - \theta_{\boldsymbol{r}}^{(-1)}}{2} + \frac{\theta_{\boldsymbol{r}+\boldsymbol{\delta}}^{(-1)} - \theta_{\boldsymbol{r}+\boldsymbol{\delta}}^{(+1)}}{2} \right) \right] \\ &= -J_\parallel \sum_{\boldsymbol{r},\,\boldsymbol{\delta}} 2 \cos \left(\frac{\theta_{\boldsymbol{r}}^{(+1)} - \theta_{\boldsymbol{r}}^{(-1)}}{2} + \frac{\theta_{\boldsymbol{r}+\boldsymbol{\delta}}^{(-1)} - \theta_{\boldsymbol{r}+\boldsymbol{\delta}}^{(+1)}}{2} \right) \left[\cos \frac{\theta_{\boldsymbol{r}}^{(+1)} - \theta_{\boldsymbol{r}+\boldsymbol{\delta}}^{(+1)} + \theta_{\boldsymbol{r}}^{(-1)} - \theta_{\boldsymbol{r}+\boldsymbol{\delta}}^{(-1)}}{2} - 1 \right], \end{aligned} \tag{2.13}$$

where we used the trigonometric expression for the sum of two cosines. The term in the square brackets is always negative and the first cosine will be positive if its argument is smaller than $\pi/2$. Therefore we have

$$E_{(a)} - E_{(b)} > 0 \quad \text{if} \quad \left| \theta_{\boldsymbol{r}}^{(+1)} - \theta_{\boldsymbol{r}+\boldsymbol{\delta}}^{(+1)} - \left(\theta_{\boldsymbol{r}}^{(-1)} - \theta_{\boldsymbol{r}+\boldsymbol{\delta}}^{(-1)} \right) \right| < \pi \tag{2.14}$$

But the argument of the first cosine is a sum of partial rotations from 0 to π between neighbouring spins, which is of course smaller than the total rotation of π. So $E_{(a)} - E_{(b)} > 0$, meaning that the energy of the "symmetric" configuration (b) (with rotation distributed equally between the 2 layers) is always smaller than that of an arbitrary spin configuration (a). This completes our proof.

Using the symmetry of the ground state and the fact that the spins can be parametrized by just one angle

$$\boldsymbol{S} = \begin{pmatrix} \cos\theta \\ 0 \\ \sin\theta \end{pmatrix}, \tag{2.15}$$

we can now re-write the Hamiltonian of Eq. (2.1) in a much simpler form (we also write the scalar products explicitly):

$$H = -J_\parallel \sum_{\boldsymbol{r},\boldsymbol{\delta}} \cos\left(\theta_{\boldsymbol{r}} - \theta_{\boldsymbol{r}+\boldsymbol{\delta}}\right) + J_\perp \sum_{\boldsymbol{r}} \cos\left(2\theta_{\boldsymbol{r}}\right) \tag{2.16}$$

Instead of two layers, we now effectively have just one layer with a self-interaction $\cos(2\theta_{\boldsymbol{r}})$. In Eq. (2.16) – and also the rest of this thesis – we assume $S = 1$. The summation over $\boldsymbol{\delta}$ is a summation over the four in-plane nearest neighbors. One might also notice that the term describing the interaction with the impurity disappeared. Since that interaction energy was much bigger than any other energy scale in the system, we now consider it to be infinitely large, and thus it acts as an effective *ferromagnetic* interaction between the two spins in the centers of the layers.

Here we have chosen our axes such that all spins lie in the xz-plane. The angle $\theta_{\boldsymbol{r}}$ of the spins at distance $\boldsymbol{r}$ from the center is measured with respect to the $\hat{\boldsymbol{x}}$-axis, which is chosen along the direction of the spins at ∞ in the upper layer. Because of the symmetry of the ground state, we have the following boundary conditions:

$$\theta_{\mathbf{0}} = \frac{\pi}{2} \tag{2.17a}$$

$$\theta_{\infty} = 0. \tag{2.17b}$$

2.2 Continuum Model

We are now interested in finding the dependence of the tilting angle θ on the distance from the center, $\boldsymbol{r}$. The easiest way to do this is to pass to the continuum model, where one assumes that the angle difference between neighboring spins is small enough to be able to expand the cosines and keep just the first two terms in this expansion:

$$\cos(\theta_{\boldsymbol{r}} - \theta_{\boldsymbol{r}+\boldsymbol{\delta}}) \approx 1 - \frac{1}{2}(\theta_{\boldsymbol{r}} - \theta_{\boldsymbol{r}+\boldsymbol{\delta}})^2 . \tag{2.18}$$

The self-interaction term in Eq. (2.16) obviously becomes

$$\frac{J_{\perp}}{a^2} \int d^2r \, \cos(2\theta(\boldsymbol{r})) \tag{2.19}$$

in the continuum limit, where a is the lattice constant. As for the first term in Eq. (2.16), substituting the expansion (2.18) of the cosine yields two terms: (i) a constant term $-4NJ_{\parallel}$[1] which is just the total energy of the ferromagnetic state and which can be dropped from the Hamiltonian and (ii) a term summing the squares of all the nearest-neighbor angle-differences. The latter can be simplified if one uses (see Fig. 2.8)

$$(\theta_{\boldsymbol{r}} - \theta_{\boldsymbol{r}+\boldsymbol{\delta}})^2 = \frac{(\boldsymbol{S}(\boldsymbol{r}) - \boldsymbol{S}(\boldsymbol{r}+\boldsymbol{\delta}))^2}{S^2}. \tag{2.20}$$

Now we can expand $\boldsymbol{S}(\boldsymbol{r}+\boldsymbol{\delta})$ for small $\boldsymbol{\delta}$'s and the zeroth order term will cancel and we get:

$$(\theta_{\boldsymbol{r}} - \theta_{\boldsymbol{r}+\boldsymbol{\delta}})^2 = \frac{1}{S^2} \sum_{\alpha,\beta} \delta^{\beta} \partial_{\beta} S_{\alpha}(\boldsymbol{r}) \delta^{\beta} \partial_{\beta} S_{\alpha}(\boldsymbol{r}) \tag{2.21}$$

[1] N is the total number of spins in a layer.

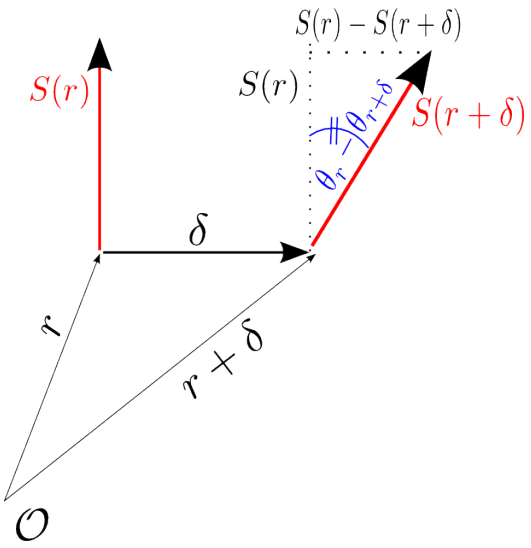

Figure 2.8: Sketch describing the relationship between two neighboring spins and their relative angle. For small angles, Eq. (2.20) can be applied. Here, $\mathcal{O}$ denotes the origin of the coordinate system.

Now we substitute (2.21) into (2.18) and the latter into the first term of Eq. (2.16). Explicitly performing the sum over the 4 δ's and then replacing the sum over $\boldsymbol{r}$ with an integral over d^2r, we finally get the whole energy in the continuum limit (using Einstein's summation convention):

$$E = J_{\parallel} \int d^2r \, \partial_\alpha S_\beta(\boldsymbol{r}) \partial^\alpha S^\beta(\boldsymbol{r}) + \frac{J_\perp}{a^2} \int d^2r \, \cos(2\theta(\boldsymbol{r})). \tag{2.22}$$

Our next goal is to look for radially symmetric (due to the boundary conditions (2.17)) solutions of the Euler-Lagrange equations

$$\delta E = 0. \tag{2.23}$$

We will now see that such solutions only exist if one introduces a cut-off.

Scale Invariance

However, before solving Eq. (2.23), let us first look at the structure of the energy in Eq. (2.22). First let's consider just the first term of Eq. (2.22). Suppose we have a solution $\boldsymbol{s}(x, y)$, with energy ϵ, for this first term. By making the transformations

$$x \to \Lambda x \tag{2.24a}$$
$$y \to \Lambda y \tag{2.24b}$$

one immediately gets that $\boldsymbol{s}(\Lambda x, \Lambda y)$ is also a solution with the same energy, since the Λ^2 factor from d^2r will be cancelled by $1/\Lambda^2$ from the two partial derivatives. Therefore

this term is scale invariant, the energy of a solution does not depend on its scale[2]. Since this trick obviously fails for the second term of Eq. (2.22), one can say that, in a sense, this term "sets a scale" to our solutions.

To conclude, we have seen that the in-plane ferromagnetic interaction is not affected by polaron size, while the inter-plane interaction will shrink the polaron to a point. Therefore there is no solution of the Euler-Lagrange equations in the continuum model. One has either to impose a boundary condition at some cut-off distance of the order of the lattice constant or, better (and that is what we will do in the next Chapter), to account for the discrete nature of the spin lattice close to $\boldsymbol{r} = 0$.

[2]Actually, in 2 spatial dimensions, scale invariance is automatically "upgraded" to conformal invariance, that is, invariance upon any transformation that does not change the angles.

Chapter 3

Results

In this Chapter we will present the main results which follow from the model of Chapter 2. These results are divided into 2 categories and first the zero-temperature case (ground state) is presented in Section 3.1, followed by the finite-temperature case (where we used Monte-Carlo calculations) in Section 3.2.

3.1 Ground State (T=0)

Let us now find the dependence of the tilting angle θ on the distance $\boldsymbol{r}$ from the center by solving the Euler-Lagrange Eqs. (2.23). We can immediately rewrite Eq. (2.22) by making use of Eq. (2.15) and get

$$E = J_{\parallel} \int dx\, dy\, \left((\partial_x \theta(x,y))^2 + (\partial_y \theta(x,y))^2 \right) + \frac{J_{\perp}}{a^2} \int dx\, dy\, \cos(2\theta(x,y)) \tag{3.1}$$

We now switch to polar coordinates in the (x, y) plane, so θ becomes a function of r and the azimuthal angle ϕ:

$$E = J_{\parallel} \int r\, dr\, d\phi\, \left((\partial_r \theta(r,\phi))^2 + \frac{1}{r^2} (\partial_\phi \theta(r,\phi))^2 \right) + \frac{J_{\perp}}{a^2} \int r\, dr\, d\phi\, \cos(2\theta(r,\phi)) \tag{3.2}$$

Actually, as explained at the end of Section 2.2, the boundary conditions dictate radial symmetry at $\boldsymbol{r} \to \infty$ for our solutions, so clearly $\partial_\phi \theta = 0$, which simplifies the above equation.

We can now finally write the Euler-Lagrange equation for the functional (3.2)

$$\partial_r \frac{\partial E}{\partial (\partial_r \theta)} - \frac{\partial E}{\partial \theta} = 0 \tag{3.3}$$

which, after simplification, yields:

$$\frac{a^2 J_{\parallel}}{|J_{\perp}|} \nabla^2 \theta(r) = \sin(2\theta(r)) \tag{3.4}$$

Eq. (3.4) has the form of an elliptic Sine-Gordon equation [14], which unfortunately has no closed form solutions for our boundary conditions (or, in other words, it has no radially symmetric solutions). However, using the fact that at infinity the angle θ is zero (see Eq. (2.17b)), we can expand the sine term at large distances r, far away from the center of the layer, and keep just the first order term, which is linear in θ. Furthermore, to make Eq. (3.4) dimensionless, we introduce the following notation

$$r_0 = a\sqrt{\frac{J_\parallel}{2\,|J_\perp|}} \tag{3.5}$$

Fortunately, the resulting equation, linear in θ, is analytically solvable, and the solution is:

$$\theta\left(\frac{r}{r_0}\right) = CK_0\left(\frac{r}{r_0}\right) \approx \frac{C'}{\sqrt{r/r_0}}\exp\left(-\frac{r}{r_0}\right) \tag{3.6}$$

where the constants C and C' appear because we are solving a second-order differential equation with just one boundary condition, the one at infinity. In Eq. (3.6), K_0 is the so-called MacDonald function (or modified Bessel function of the second kind) [15], which diverges when its argument is 0 and decays exponentially for large arguments. In the asymptotic expansion of the MacDonald function on the right hand side of Eq. (3.6), we see that the scale of our solution is given by r_0. The ratio between the two interactions which appear in the expression (3.5) for r_0 determines the size of the actual solution. Note once again that the scale r_0 only appears once we impose the condition that $\theta = \pi/2$ at some cut-off of the order of the lattice constant a. If we would impose the condition that $\theta(0) = \pi/2$, we would get no solutions for the Euler-Lagrange equations.

3.1.1 Matching with Discrete Model

It is clear that the validity of the solution given by Eq. (3.6) will only be far away from the core of the spin polaron. In order to determine the full solution one has to solve (minimize the energy of) the discrete Hamiltonian (2.16) in a small square region close to the center of the layer (see Fig. 3.1). By matching the discrete and continuous solutions along the perimeter of the inner square, we also determine the value of the constant C. In fact, it turns out that the angle differences between successive spins close to the centre of the spin polaron are quite large, which means that the continuum model is not even applicable in that region, and our approach is fully justified.

In practice, we start from the edges of the layer and analytically compute the angles θ outside the checkerboard square (see Fig. 3.1). Since for practical reasons this square cannot be made very large, we have to take into account also higher harmonics of the continuous solution which are consistent with the symmetry of the lattice:

$$\theta\left(\frac{r}{r_0}\right) = C_0K_0\left(\frac{r}{r_0}\right) + C_4K_4\left(\frac{r}{r_0}\right)\cos(4\phi) + C_8K_8\left(\frac{r}{r_0}\right)\cos(8\phi) + \ldots, \tag{3.7}$$

where ϕ is the polar angle. Inside the checkerboard square we compute the angles by minimizing the energy of the discrete model, Eq. (2.16). This still leaves us with the

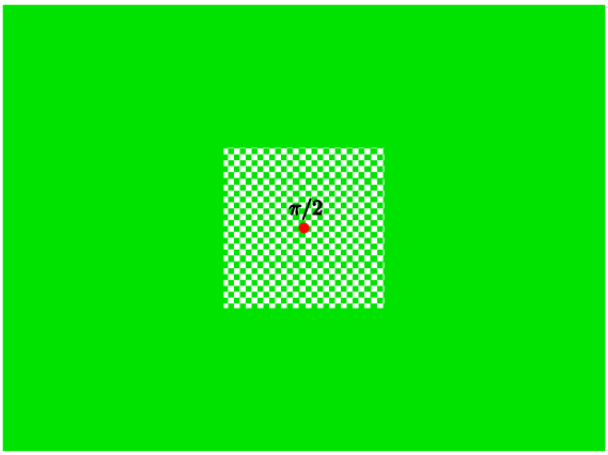

Figure 3.1: Matching of discrete and continuum solutions. Green rectangle represents layer of spins. Starting from the edge of the layer up to the boundary of the checkerboard square, we calculate the angle θ using Eq. (3.6). Inside the square, we calculate the angles by minimizing the energy given by the discrete Hamiltonian Eq. (2.16).

unknown constants C, which we simply determine by imposing the condition that the angle in the centre should have a value of $\pi/2$. The final result for the ground state is shown in Fig. 3.2.

We have also plotted the profiles of various spin polarons obtained by varying the ratio $h = J_\perp/J_\parallel$ in Figure 3.3. As expected, we see that the polarons increase in size as the ratio h decreases.

It is now interesting to examine a plot of the magnetization carried by these spin textures. Figure 3.4 shows this magnetization as a function of the ratio h. The interval chosen for varying h is the same as the one of Fig. 3.3. It is important to emphasize that magnetization, in this context, refers of course to the parallel component of the total magnetization, the one along the direction of the layer. It is obvious that the perpendicular component will cancel, since the projections of the spins on the vertical axis are equal and opposite from layer to layer.

Examining Fig. 3.4, we see the dramatic increase of magnetization produced by increasing spin polaron size. This shows that the polarons can carry a very large magnetization and (since the directions of the spins involved will fluctuate at nonzero temperatures) this explains the appearance of the superparamagnetic state in the phase diagram Fig. 1.12.

3.2 Finite Temperatures

All the results presented so far were obtained for the ground state. For finite temperatures it is very difficult to tackle the problem analytically due to the huge number of degrees of freedom involved. Therefore, our approach was to find out useful information about the system through the help of numerical Monte-Carlo simulations [16].

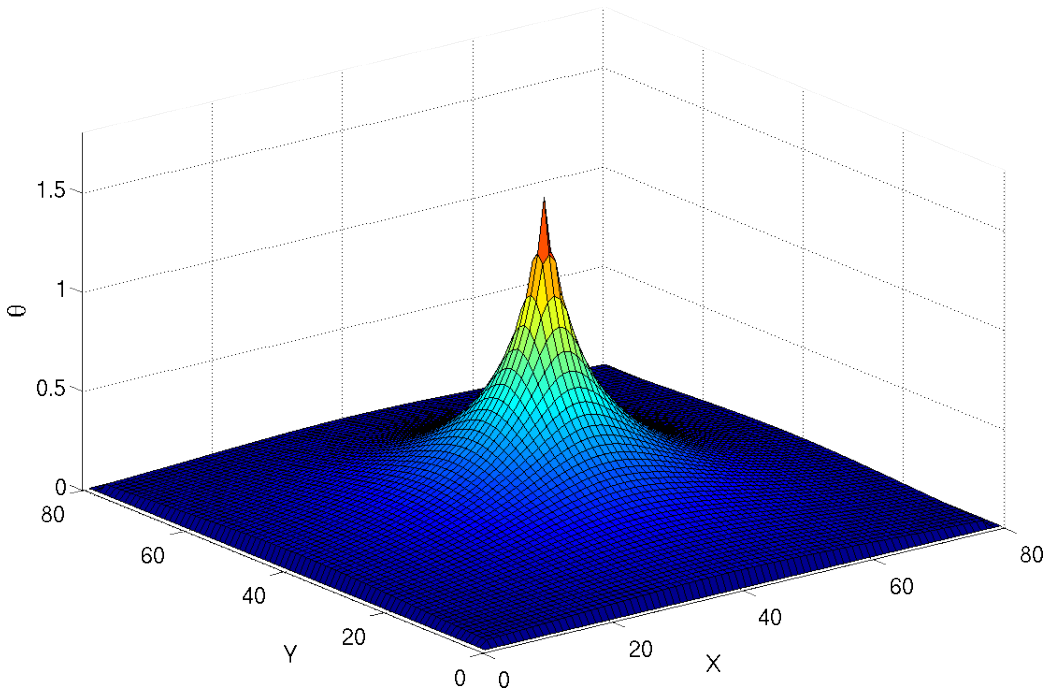

Figure 3.2: Numerical surface plot of the angle θ as a function of coordinates in the (X, Y) plane for an 80×80 lattice. We chose a rather small value of $h = \frac{J_\perp}{J_\parallel} = 0.001$, so the spin polaron sits almost on the system size. The value of the angle in the centre is $\pi/2$. Notice the large difference in angles close to the core, which limits the applicability of the continuum model. The upper layer can be constructed using the symmetry of the ground state, as explained in Section 2.1.2.

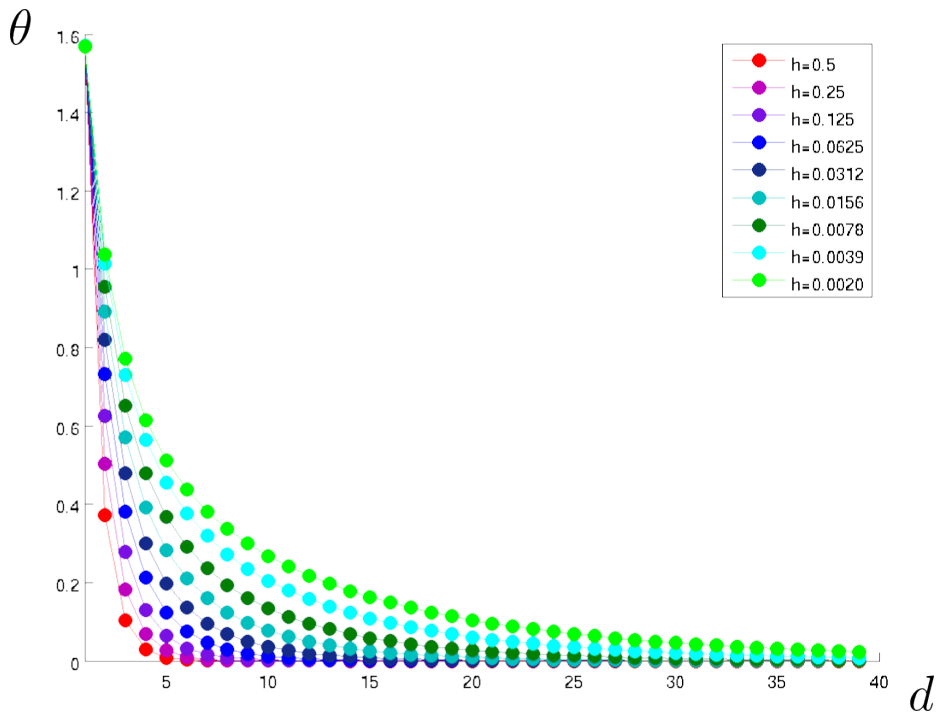

Figure 3.3: Profiles of various spin polarons on a square layer of 40×40 sites. The angle θ is plotted as a function of the distance d (measured in lattice sites) from the centre of the layer. The different colours correspond to different values of the ratio $h = \frac{J_\perp}{J_\parallel}$. Notice that, as h decreases (from red to green), the size of the spin polaron increases (as expected).

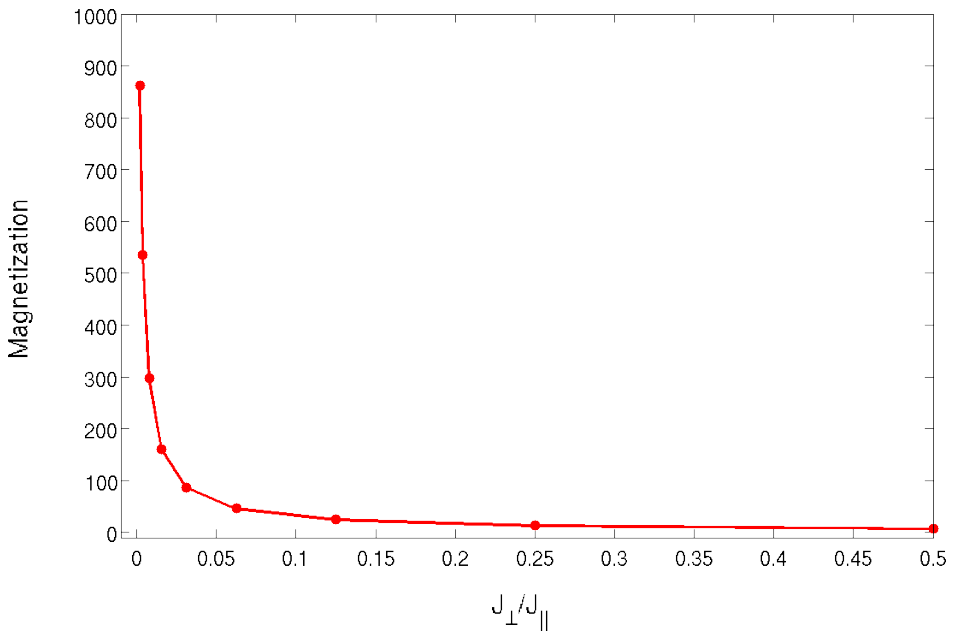

Figure 3.4: Plot of the parallel component of the magnetization as a function of the ratio $h = J_\perp/J_\parallel$, for the same range of values of h as in Fig. 3.3. The magnetization increases as a power of h with decreasing h (increasing spin polaron size) and actually diverges for $h \to 0$. This proves that the polarons are capable of carrying a very large magnetization.

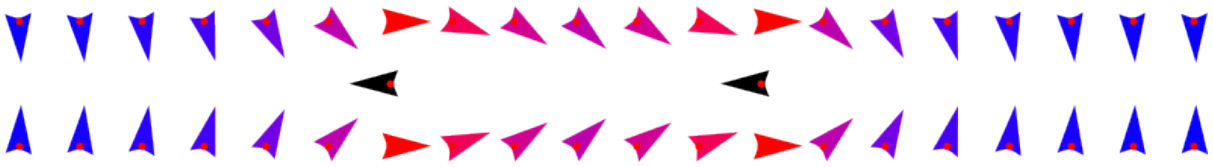

Figure 3.5: Let us now consider two layers (side view) with two Fe impurities in between (shown in black here). They both induce polarons in the above and below layers, where the spins are coloured proportional to their deviation from the vertical axis. The spins of the impurities are labeled by $\boldsymbol{S}_1$ and $\boldsymbol{S}_2$, and we are interested in their effective interaction through the induced polarons.

We are particularly interested in the indirect, effective interaction between two impurities, through the spin polarons that they both induce in the layers above and below (see Fig. 3.5).

If we denote this effective interaction by J_{eff}, we can immediately write down the standard statistical physics expression for their correlator at a given temperature T [17]:

$$\langle \boldsymbol{S}_1 \boldsymbol{S}_2 \rangle = \coth\left(\frac{J_{\text{eff}}}{T}\right) - \frac{T}{J_{\text{eff}}} \tag{3.8}$$

We calculated this correlator through a Metropolis Monte-Carlo algorithm, and plotted the result for four different temperatures in Figure 3.6. The correlator was calculated as a function of distance between impurities, stating with a separation of one lattice site and then gradually increasing it. It is now straightforward to invert Eq. (3.8) and express the effective interaction J_{eff} in terms of the spin-spin correlator $\langle \boldsymbol{S}_1 \boldsymbol{S}_2 \rangle$. The result is plotted in Fig. 3.7. The result is quite clear: the effective interaction between impurities is ferromagnetic and it grows as the distance between them decreases. This can explain the ferrimagnetic part of the phase diagram in Fig. 1.12. We also see that the interaction between impurities decays at a distance on the order of 10 lattice sites.

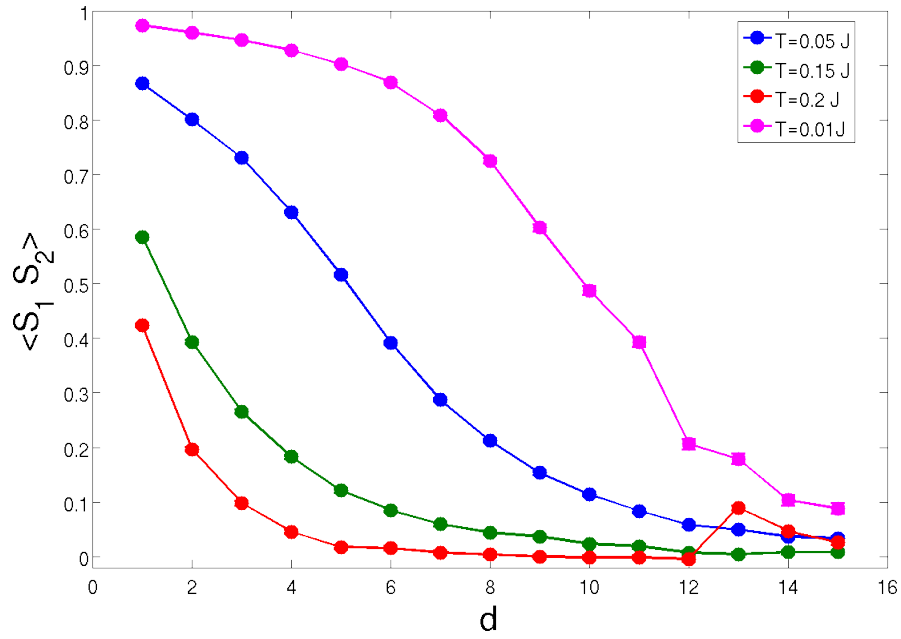

Figure 3.6: Plot of correlator between the two impurity spins as a function of their distance d, measured in lattice sites. The four curves correspond to four different temperatures, as noted in the inset. The plot was obtained by running successive Monte Carlo simulations. The presence of a hump at $d = 13$ is due to the fact that the respective simulation did not run for long enough to converge.

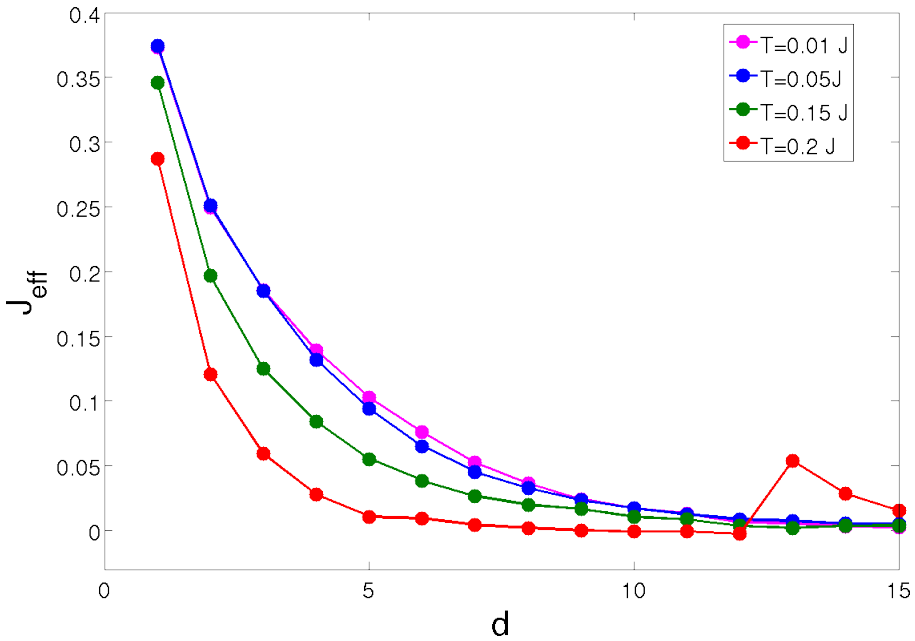

Figure 3.7: Plot of the effective interaction between the two impurities as a function of the distance between them, obtained by inverting Eq. (3.8) and using the Monte-Carlo results for $\langle \boldsymbol{S}_1 \boldsymbol{S}_2 \rangle$ from Fig. 3.6. The same set of 4 temperatures as in Fig. 3.6 was used. We see that the interaction is ferromagnetic and gets very strong as the impurities are brought close together.

Chapter 4

Conclusions

The solid solution (1-x)$FeTiO_3$–(x)Fe_2O_3 of the two antiferromagnetic compounds, $FeTiO_3$ (ilminite) and Fe_2O_3 (α-hematite), exhibits an unusual insulating ferrimagnetic state appearing around room temperature, for a range of concentrations x between 0.2 and 0.6. This state is potentially important for applications. We have qualitatively explained the most relevant parts of the phase diagram of this compound, shown in Fig. 1.12.

We have shown that Fe dopants in Ti layers induce large non-collinear modulations of spins in neighboring magnetic layers, which we refer to as spin polarons.

We studied the magnetic properties of these spin polarons and their effect on the magnetic properties of (1-x)$FeTiO_3$–(x)Fe_2O_3. The first key result is that these co-planar spin configurations are energetically favourable, having a lower energy than skyrmions in this system. However, skyrmions may still be present as excited states, since they are allowed by the boundary conditions.

Another key result is that these polarons can carry a very large in-plane magnetic moment, resulting in superparamagnetic behavior of the magnetic susceptibility in the antiferromagnetically ordered phase (for very small concentrations x).

By further increasing the concentration x, one gets to a regime where the spin polarons start overlapping. More impurities means that the average distance between them will be smaller, hence the ferromagnetic coupling J_{eff} will be larger. We have seen how the long-range ferromagnetic interaction between the spins of the Fe impurities, mediated by overlapping spin polarons in neighboring magnetic layers, can give rise to an antiferromagnetic-to-ferrimagnetic transition at relatively low concentrations x.[1]

We also understand the linear decrease in the experimental plot of magnetization vs concentration, Fig. 1.13. Once x gets close to 0.2, the magnetization has its peak value, meaning that all the spin polarons are aligned in the same direction. By further adding of Fe impurities (increasing x), one is effectively adding spins which point in the opposite direction to those of the polarons, thereby linearly decreasing the overall magnetization of the system.

[1]The state will be ferri(and not ferro)magnetic because there is still a small number of impurities which will have the spins pointing in the opposite direction to the polarons (see Fig. 3.5).

The only physically interesting region of the phase diagram which we have not yet explained is the spin-glass state.

Chapter 5

Outlook

As in any scientific research project, there are always still plenty of things left to be done.

Throughout this thesis, we have completely neglected the different valencies of the two types of Fe ions involved, Fe^{2+} and Fe^{3+}. Apart from them having different values of the spin quantum number, this implies also the presence of a mobile hole in this material, which we also neglected. This mobile hole seems to be localized, since the solid solution is insulating [18]. However, experimentalists have also recently observed an enhancement of the dielectric constant below room temperature, which would be a good starting point for further investigations.

As already mentioned in the conclusions, another possible research topic would be to find an explanation for the presence of the spin-glass state at small concentrations and temperatures in the phase diagram (see Fig. 1.12).

The last point (which we already working on) is a complete **quantitative** explanation of the phase diagram of (1-x)$FeTiO_3$–(x)Fe_2O_3, by a full numerical Monte-Carlo calculation of a larger number of layers and impurities at different temperatures and varying the impurity concentration.

Bibliography

[1] J. M. Ziman. *Principles of the Theory of Solids*. Cambridge University Press, 1979.

[2] C. Kittel. *Quantum Theory of Solids*. Wiley, 1987.

[3] Sawatzky G. A. Khomskii D.I. *Solid State Communications*, **102**:87–99, 1997.

[4] S. Blundell. *Magnetism in Condensed Matter*. Oxford University Press, 2001.

[5] J.B. Goodenough. *Magnetism and the Chemical Bond*. R. E. Krieger Pub. Co, 1976.

[6] J. Hemberger, A. Krimmel, T. Kurz, H.-A. Krug von Nidda, V. Yu. Ivanov, A. A. Mukhin, A. M. Balbashov and A. Loidl. *Phys. Rev. B*, **66**(9):094410, Sep 2002.

[7] Clarence Zener. *Phys. Rev.*, **82**(3):403–405, May 1951.

[8] D. C. Mattis. *The Theory of Magnetism Made Simple*. World Scientific Publishing, 2004.

[9] Y. Ishikawa and S. Akimoto. *Journal of the Physical Society of Japan*, **12**:1083–1098, 1957.

[10] Y. Ishikawa, N. Saito, M. Arai, Y. Watanabe and H. Takei. *Journal of the Physical Society of Japan*, **54**:312–325, 1985.

[11] G. E. Brown, editor. *Selected Papers With Commentary of Tony Hilton Royle Skyrme*. World Scientific, 1994.

[12] A. A. Belavin and A. M. Polyakov. *JETP Lett.*, **22**:246, 1975.

[13] S. L. Sondhi, A. Karlhede, S. A. Kivelson and E. H. Rezayi. *Phys. Rev. B*, **47**(24):16419–16426, Jun 1993.

[14] R. Rajaraman. *Solitons and Instantons*. North-Holland Personal Library, 1989.

[15] M. Abramowitz and I. A. Stegun, editors. *Handbook of Mathematical Functions with Formulas, Graphs, and Mathematical Tables*. New York: Dover, 1965.

[16] M. Troyer. Classical and quantum monte carlo algorithms. http://research.yale.edu/boulder/Boulder-2004/ReadingMaterial-2004/QMC_ED.pdf.

[17] L. D. Landau and E. M. Lifshitz. *Statistical Physics*. Butterworth-Heinemann, 3rd edition, 1984.

[18] Y. Ishikawa. *Journal of the Physical Society of Japan*, **13**:37–42, 1958.

Appendix A

Acknowledgements

I would like to thank my adviser Maxim Mostovoy for his guidance and for bringing this fascinating field to our attention.

Thanks especially to my collaborators, Sergey Artyukhin and Andrea Scaramucci, without whom this would not have been possible.

I would also like to thank Elisabetta Pallante for taking the trouble to proofread this thesis.

Last but not least, I am indebted to the Zernike Institute for Advanced Materials and the University of Groningen for supporting the Top Master Programme in Nanoscience.